HOST UNIVERSITY: Ghent University

FACULTY: Faculty of Engineering and Architecture

DEPARTMENT: Department of flow, heat and combustion
Academic Year 2017-2018

Numerical simulations of flame spread in a combustible corner

Fearghál Gill

Supervisors:

Prof. Bart Merci, Ghent University
Dr, Georgios Maragkos, Ghent University

Master thesis submitted in the Erasmus+ Study Programme
International Master of Science in Fire Safety Engineering

ABSTRACT

The use of engineered timber products has in recent years begun to increase in part due to environmental concerns but also in part due the speed of erection of timber buildings. A worry with this trend is due to the combustible nature of wood-based products. One does not require to dig too far back in the past to find examples of notable fires in which flame spread rapidly throughout the building. Historically testing procedures have been developed to try and determine the behaviour of building products under fire conditions. There has been an observed disparity between results of bench-scale and large-scale test due to the coupling of various complex physical processes. However, work is being conducted in the field of computational fluid dynamics (CFD) to link these two scales.

The work presented herewith is a continuation of experimental and numerical work on engineered products carried out at the Ghent University. In that work calcium silicate, MDF and Plywood panels were tested to requirements of the Single Burning Item (SBI) test procedure and were then subsequently simulated using the FireFoam computational fluid dynamics (CFD) package. This work attempts to use the Fire Dynamics Simulator (FDS) CFD code version 6.7.0 to simulate the response to fire of both the inert calcium silicate and plywood tests. The pyrolysis parameters of the plywood panels used in the work were previously determined via the inverse modelling of Fire Propagation Apparatus bench scale test in a nitrogen environment using the 1-dimensional pyrolysis model in the FireFoam package. An emphasis of this study is on the influence of the convective heat transfer models.

The calcium silicate simulations show that the flame heights are overpredicted for the triangle burner whilst the heat fluxes at three distinct locations on the panels were underpredicted. The inaccuracy of the heat flux predictions increased at locations further away from the corner. The choice of convective heat transfer model did not have a significant influence on the results although the wall model produced slightly higher heat fluxes and thus providing a more accurate result. Using the default model effective parameters for the plywood cases greatly over-predicted the total heat release rate when compared with the experiments. A sensitivity analysis was undertaken by varying the heat of combustion and the heat of reaction two significant parameters influencing the HRR. Significant overprediction of the HRR is still observed when varying these input parameters. Similarly, to the calcium silicate case, the heat fluxes are underestimated in each of the three locations with flame heights also being overpredicted. It can be deduced from these simulations that the model effective parameter previously derived are not suitable to accurately predict the fire behaviour of plywood in a corner configuration.

Acknowledgments

I would like to thank my thesis supervisor Dr. Georgios Maragkos for his guidance throughout my research. His expert knowledge and illuminating responses significantly influenced the course of this study. I would also like to thank the entire IMFSE consortium who have been extremely accommodating throughout these past few years leading to an incredibly joyous experience.

Table of Contents

Table of Figures

1 <u>INTRODUCTION</u>

Despite the noticeable improvements in fire safety over the last few decades with the introduction of building regulations and testing procedures fire remains a threat to life and property whenever it occurs. This is shown harrowingly with recent fires that have been in the public consciousness such as the 2017 Grenfell Tower Fire in which 72 people lost their lives [1], the 2018 Kemerovo fire which killed at least 60 people [2] and the 2019 Notre Dame fire which significantly damaged a famous heritage and cultural site in France [3].

Whilst there have been great improvements in fire safety standards, combustible products are still used within the construction industry due in part to cost requirements but also out of shear practicality. In recent years there has been a trend towards sustainable building practice with the use of timber and engineered timber products increasing in use [4,5]. This is due largely to environmental concern along with the speed of construction for timber structures being notably quicker than conventional methods [5]. Currently there are number timber skyscrapers being proposed in London, England along with a multitude of other high rise timber buildings in Europe [6]. This new trend whilst environmentally beneficial will also have some difficulties in terms of fire safety. An inherent property of timber products is its combustible nature, which could potentially exacerbate the impact of a fire. This trend along with the damage incurred in previous fire shows the importance of understanding how fire propagates and whether the spread of fire can accurately be predicted.

Fire and flame spread are extremely complex processes which involves a variety process such as heat transfer, turbulence along with physical/chemical reactions in the solid and gas phase. The interaction between these processes be extremely non-linear and turbulent [7,8] with the geometry surrounding the fire having noticeable impact on flame spread. Corner fires, in particular, have been observed to exacerbate a fire due to flame extension due, reduced entrainment of air and the radiative feedback mechanism that occurs between the walls in the corner.

As a means of characterising the behaviour of fire for different materials testing procedures have been developed. Common test procedures are the bench scale Fire Propagation Apparatus (ASTM E2058) test and Cone Calorimeter Test (ISO 5660-1), the intermediary Single Burning Item (EN 13823) test and the large-scale ISO Room Corner test (ISO 9705). Due to the scale of the SBI and ISO Room Corner tests large test specimens are required, these tests also require multiple tests to determine the reproducibility of the fire behaviour. This would naturally incur a large economic cost to manufactures. There has been many studies that have investigated the impact of combustible corners on a fire with empirical correlation being developed to quantify it [9,10]. Whilst these correlations may be useful to approximate the impact, they do not present the full picture of a corner fire. The cost requirement of performing test show that it would be extremely beneficial if data collected from bench scale tests could be used in conjunction with Computational Fluid Dynamics (CFD) packages to predict the behaviour of intermediate to larger fire scenarios.

This study aims to simulate the flame spread of plywood boards when tested in accordance with the SBI test EN 13823 by using the Fire Dynamics Simulator (FDS) v6.7.0. FDS is a CFD package developed by NIST [11]. The work will build on previous experimental and numerical work carried out in UGent [12–16]. In the experimental work inert calcium silicate boards, MDF and plywood boards were exposed to a triangle burner with the impact of the fire being assessed through video imagery, heat flux gauges and thermocouples.

When attempting to simulate the flame spread or fluid flow in general over a wall, researchers will either try to directly resolve the convective heat transfer [17–19], model it through empirical relations for the Nusselt number [20–23] or via wall functions [12]. To directly resolve the convective heat transfer computational grid sizes in the magnitude of millimetres are required to sufficiently grid resolve the near wall flow and flame scales, this is an extremely computationally expensive process. The empirical correlations and wall model methods in comparison are computationally inexpensive and are not strongly grid dependent. Further difficulties are introduced when considering convective heat transfer due to the coupling of solid phase reactions and gas phase reactions that occur in a fire. In combustible walls the production of pyrolysis gases result in what is known as the blowing effect which reduces the convective heat transfer due to the flow of the pyrolyzed gases being in the opposite direction to the flow of the fire plume. In conjunction with convective heat transfer there are different methods that are utilised to model the pyrolysis process in flame spread. A simple model was utilised in [20,21] in which the spread of flame was defined by simple input parameters such as the ignition temperature, burning rate, heat of gasification and heat of combustion. This method assumes a spatially independent burning rate it was found that this did not accurately replicate the transient total heat release rate of the experiment. When compared with experimental data this method underpredicted the flame spread in the vertical direction. A more commonly used method when studying the flame spread over a surface is by considering a pyrolysis model where a single step Arrhenius reaction is applied [12,14,23]. In this method the reaction kinetics such as the pre-exponential factor (A), activation energy (E) and heat of reaction must be specified.

There have been previous attempts to simulate the SBI test using CFD packages such as FDS and the FireFoam CFD package developed by FM Global [9,12,14,24]. It was observed in [9] simulating the SBI test is much more difficult in comparison to the ISO room test due to the quantification of the heat losses and the effect of the applied boundary conditions. The results in these simulations began to diverge significantly from the experimental results at times corresponding to the thermal penetration time of the material. In the work of [12,14] which this work aims upon, model effective parameters of MDF panels were utilized which were developed by the inverse modelling of FPA tests in nitrogen. A single step Arrhenius reaction was used to model the pyrolysis of the MDF whilst an empirical wall function was used to model the convective heat flux which considered the blowing effect induced by pyrolysis. These simulations despite the non-uniform mass density of the MDF panels predicted the heat release rates reasonably well. The other important parameters such as instantaneous flame heights, heat fluxes and pyrolysis front were also predicted to a reasonable degree. A simplified computational domain was used in these simulations which would reduce the computational time. It was observed in a further study that when FDS is used the heat fluxes at distances remote from the corner are significantly under predicted and that the inclusion of entire testing geometry results in only 'slightly' more accurate results [23].

The primary objectives of the numerical simulations are to:

- Simulate the thermal attack from the triangle burner on the inert calcium silicate walls and examine how reasonably is the fire dynamics and thermal response predicted by FDS.
- Investigate the accuracy of the convective heat flux models utilized in FDS. Determine how the models influence the thermal attack on the panels from the triangle burner.

- To simulate the plywood experiments, by the use of model effective parameters developed by the inverse modelling of FPA tests provided in [12], and investigate the influence of the gas phase grid size on the simulation results.

1.1 Outline of Thesis:

Chapter 2 will discuss all the relevant background information regarding the fundamental concepts which apply to flame spread. A summary of the influence of the heat transfer processes of conduction, convection and radiation are discussed including the areas in a fire were these processes dominate. The solid phase pyrolysis is discussed along with the subsequent gas phase processes that can follow such as the ignition above the solid and subsequently the development of a fire plume. The impact that a corner configuration has on the above processes is also discussed.

The third chapter provides a brief introduction to the development of CFD to predict fire scenarios. The governing equations that describe fluid flow such as the continuity equation, conservation of momentum and the energy equations are discussed. The numerically methods in which these equations are solved in Large Eddy Simulations is discussed along with the source terms that need to be solved.

In chapter 4 details of the SBI test procedure will be described including a general description of test conditions, the geometric layout, details on the fire size and how measurements were taken along with any limitations that were observed.

All the relevant computational details will be provided in chapter 5, including the computational domain, geometry and boundary conditions. This will include the solution procedure that FDS employs to model the source terms that were discussed in chapter 3 along with pyrolysis process reaction details.

Chapter 6 presents the results and discussion of the numerical simulations. The simulations are assessed on their ability to replicate the key parameters of the SBI test such as heat release rate, flame heights and horizontal flame front. The similarities and differences between the results will be discussed along with the errors associated with the calculations being discussed.

Finally, in chapter 7 the conclusion of the numerical simulations will be presented. There will be a brief discussion outlining the key findings and recommended future work to be studied.

2 <u>FLAME SPREAD</u>

The spread of flame over a solid surface is the process which involves a moving flame front in the pyrolysis region, it is critical to the growth and development of a fire in a building. As mentioned previously it is an extremely complex which involves a variety of interacting processes including heat transfer, fluid dynamics, physical and chemical reactions along with the interaction of these processes with the geometry. This chapter will aim to summarize the predominant processes involved in flame spread. Further in-depth discussion of these topics can be found in any fire such as the Fundamentals of fire Phenomena by James Quientiere.

2.1   Heat transfer

Heat transfer is the transfer of energy that occurs due to a difference in temperature. There are three modes of heat transfer known as conduction, convection and radiation. At a given stage or location of fire development one of the modes heat transfer will be the dominant mode [8]. Each of these three methods are summarised below.

2.1.1   Conduction

Conduction is the mode of heat transfer typically associated solids. Conduction requires a medium, this medium can be either solids, liquids or gases. The transfer of energy through a medium can be understood via Fourier's Law of Conduction (Equation 1) for a one-dimensional homogenous object.

$$\dot{q}''_x = -k\frac{\Delta T}{\Delta x} \ (Equation \ 1)$$

where $\dot{q}''_x$ is the rate of heat transfer via conduction (kW/m^2), k is the thermal conductivity of the medium (kW/m·K) and ΔT/Δx is the spatial derivative of the temperature.

As shown in equation 1 the transfer of heat through a body is proportional to the temperature gradient and that the heat transfer will be lower for materials of low thermal conductivity as opposed to materials of high conductivity. Conduction is important when trying to understand solid phase processes such as pyrolysis, ignition and subsequently flame spread.

2.1.2   Convection

Convection is the mode of heat transfer associated with the transfer of heat to or from a solid through a fluid when it is undergoing a bulk motion. There are two major assumptions when considering fluid flow over a surface, these are the no slip condition and the no temperature jump condition. The no slip condition stipulates that the velocity of the flow is zero at the wall with the no temperature jump condition stating that the temperature of the fluid and surface are the same at the point of contact.

Due to these conditions, regions develop for the flow known as thermal and velocity boundary layers. The velocity boundary layer is defined as the distance from the where the velocity is 99% that of the free stream velocity. The thermal boundary layer is similarly defined as the distance from the wall where the temperature is 99% of the temperature difference between surface and ambient temperature. At distances smaller than the velocity boundary layer there will sharp velocity gradients similarly at distances smaller than the thermal boundary layer

sharp temperature gradients are evident. Considering this heat transfer from the solid to the fluid (or vice versa) is through pure conduction due to the zero velocity at the wall.

There are a series of non-dimensional numbers that are commonly used to characterise the flow of a fluid. A study of these numbers can indicate the transition of laminar flow into a turbulent flow. These number in order of appearance are the Reynold number, Grashof number and the Prandtl number.

$$\text{Re} = \frac{uL}{v} = \frac{Inertial\ forces}{Viscous\ Forces}\ (Equation\ 2)$$

The Reynolds number is the ratio of inertia forces and the viscous forces in a flow. A large Reynolds number signifies that inertia forces dominate which indicates the transition from laminar to turbulent flow could occur.

$$Gr = \frac{g\beta(T_s - T_\infty)L}{v^2} = \frac{Buoyancy\ forces}{Viscous\ Forces}\ ;\ \beta = \frac{1}{T_\infty}\ (Equation\ 3)$$

The Grashof number is similar to the Reynolds number although it is specifically applied to free convective flows (see below) The number represents the ratio of buoyancy forces to viscous forces. When the buoyant forces overcome the viscous forces, the flow will begin to transition from a laminar flow to a turbulent flow.

$$\text{Pr} = \frac{v}{\alpha} = \frac{Molecular\ diffusivity\ of\ momentum}{Molecular\ diffusivity\ of\ heat}\ (Equation\ 4)$$

The Prandtl number is ratio of molecular diffusivity/kinematic viscosity to thermal diffusivity. When the Prandtl number is small heat diffuses very quickly in comparison to the velocity.

In the equations above, u is the velocity of the flow (m/s), g is the acceleration due to gravity (m/s^2), v is the kinematic viscosity (m^2/s), α is the thermal diffusivity (m^2/s), T_s is the surface temperature (K), T_∞ is the ambient temperature (K) and L is the characteristic length (m). For a flat surface, the characteristic length is taken as the distance from the leading edge for a vertical plate and in the case of a sphere it is taken as the diameter.

Convection can be expressed in a macroscopic manner by Newtons law of cooling/heating:

$$q''_{conv} = h\Delta T = h(T_g - T_s)\ (Equation\ 5)$$

where $\dot{q}''$ is the rate of heat transfer via convection (kW/m^2), h is the convective heat transfer coefficient (kW/m^2·K) and ΔT is the temperature difference between the solid and the fluid.

The value of h is not a thermodynamic property, but an empirical parameter determined by the fluid properties, geometry and the flow conditions. Considering this the convective heat transfer coefficient defined by the Nusselt number:

$$Nu = \frac{hL}{k}\ (Equation\ 6)$$

where k is the thermal conductivity of the gas (W/m·K).

Empirical correlations have been developed which can be used to calculate the Nusselt number. There correlations are dependent on whether convection is free or forced. Forced convection occurs when the motion of the fluid is not primarily caused by the heat transfer process but through an external agent (e.g., fans or pumps). In contrast with forced convection, free convection will occur due to heat transfer process itself. Depending on the type of convective, the Nusselt number is either a function of the non-dimensional Reynolds and Prandlt numbers for forced convection or of the Prandtl and non-dimensional Rayleigh number for free convection. Typical convective heat transfer values for free convection range between 5-25 W/m^{2}K with forced convection ranging anywhere up to 1000 W/m^{2}K [25]. Experimental correlations for Nusselt number for both free (equation 7) and forced (equation 8) convection over a vertical plate are displayed below:

$$Nu = \frac{hL}{k} = \left(0.825 + \frac{0.387 Ra^{\frac{1}{6}}}{\left[1 + (0.492/Pr)^{\frac{9}{16}} \right]^{\frac{8}{27}}} \right)^{2} \quad (Equation\ 7)$$

$$Nu = \frac{hL}{k} = 0.228 R\,e^{0.731} Pr^{\frac{1}{3}} : \quad 4000 < Re < 15{,}000 \ (Equation\ 8)$$

$$Ra = GrPr \ (Equation\ 9)$$

Convective heat transfer whilst important in all aspects of fire development is particularly important at the beginning stages of the fire as radiation effects will not be as prominent due to the lower temperatures (see section 2.1.3). In a fire situation the convective heat transfer is mainly due to the fire plume interacting with the surroundings which as per the no temperature jump condition will have significant temperature gradients within the thermal boundary layer. Further downstream any small disturbances in the flow can be amplified (inertia forces dominate) causing the transition of a laminar flow into a turbulent flow. An example of a flow over a vertical plate is shown in figure 1.
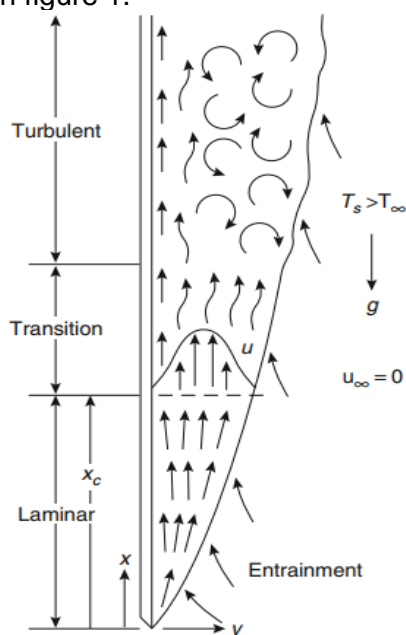

Figure 1 Development of turbulence in a vertical wall flow. Reproduced from [24]

The laminar zone of fluid motion is well ordered with streamlines being identifiable within it. The turbulent zone in contrast is highly irregular and consists of velocity fluctuations which enhance momentum and energy transfer. The momentum and energy transfer will cause the convective heat transfer to be higher when compared to the laminar zone. The velocity fluctuations will cause the mixing of the fluid and ambient air increasing the thickness of the turbulent layer, within this turbulent layer averaged profiles of velocity, temperature and concentration are flatter than in laminar flow however steep temperature and velocity gradients will still be between the fluid and wall.

2.1.3 Radiation

Thermal radiation is the mechanism by which remote objects get heated and potentially ignite at a distance from the fire source. It is different to conduction and convection in that it requires no medium in order to transmit energy via electromagnetic waves. The energy emitted by a body is given by the Stefan-Boltzmann law:

$$E = \epsilon \sigma T^4 \ (Equation\ 10)$$

where E is the total emissive power (kW/m^2). Whilst the percentage of heat flux received by a body is given by:

$$q''_{rad} = F \epsilon \sigma T^4 \ (Equation\ 11)$$

where ϵ is the emissivity of the body (-) taken as 1 for a blackbody, σ is the Stefan-Boltzmann constant (5.67 x 10^{-11} kW/m^{2}K^4), T is the absolute temperature of source (K), q''_{rad} is the heat flux by radiation received by a body (kW/m^2) and F is the configuration/view factor(-), The value of F is dependent on the relationship between the geometry of the emitter with correlations for different geometries found in and fire related textbook.

As the heat flux due to radiation is directly proportional to T^4 it is evident that radiation effects will not be as influentially during the growth stage due to the relatively low temperatures in comparison to when the fire is more developed.

2.2 Pyrolysis

Pyrolysis is the process in which a combustible solid will thermally degrade and produce gaseous fuel above the surface of the fuel [27]. When a solid material, initially at ambient temperature, is subjected to an external source of heat energy the temperature of the solid will start to increase. This temperature will first rise on the surface and then transfer through the body via conduction. The rate of temperature rise throughout the body is dependent on the magnitude of the heat transferred to the body and on the solids ability to resist the temperature rise. A solids resistance to temperature rise is characterised by its thermal inertia $k\rho c$ which is the product of the materials density, thermal conductivity and heat capacity of the solid. After a certain time of exposure to a heat flux (t$_p$) and surface temperature (T$_p$) the solid will begin to thermally decompose/pyrolyze and produce flammable vapours. The pyrolysis process transforms solid fuel into the gas phase by the breakdown of molecules into different smaller molecules. [8].

The volatiles produced by pyrolysis are a complex mixture of simple molecules to species of high molecular weight [8]. In flaming combustion these products will be consumed by the

flame. Within the solid the production of gaseous fuel can occur in a variety of different manners such as sublimation in which the fuel vapours are produced directly from the solid without going through a liquid phase when exposed to a heat source. The material can also melt into a liquid form and then further decompose by pyrolysis and produce further fuel vapours.
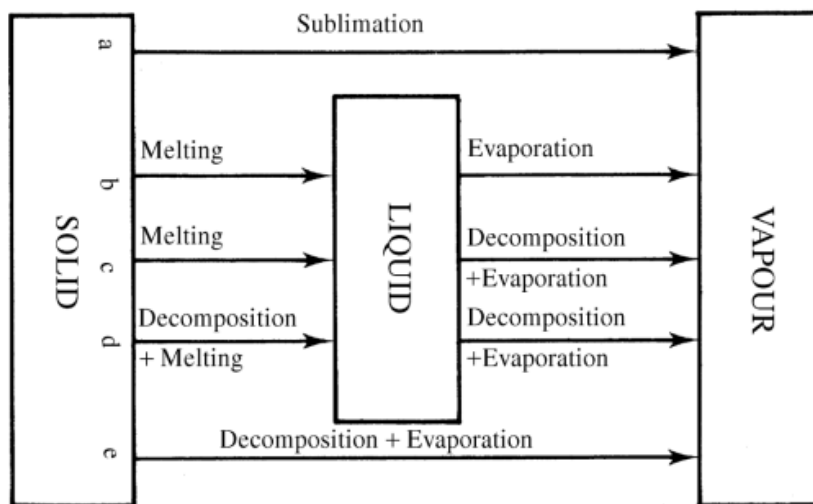
Figure 2 Modes that fuel vapour can be generated from a solid fuel. Reproduced from [8].

The solid phase kinetics tend to follow an Arrhenius equation where the reaction rate is a function of the temperature of the solid, the pre-exponential factor A (s⁻¹) and the activation energy E (J/mol) [28]:

$$r = Ae^{\left(\frac{E}{RT}\right)} \ (Equation \ 12)$$

Typically, when timber is exposed to a heat source it will first begin drying once the temperature exceeds 100°C. After the drying the timber will decompose producing volatile species at temperatures in the range 200-300 °C and leaving a solid residue known as char [29]. This char will have an influence on the heat transfer through the fuel and the mass transfer of products from inside the solid to the surface. The char produced is usually composed of carbon and can be further pyrolyzed producing more flammable vapours when this decomposition occurs at temperatures in excess of 300 °C. This process can either be complete producing ash or require further decomposition. In comparison to non-charring materials, char can reach significantly higher temperatures and can be the ignition source gas phase combustion (see section 2.4). [27,29]

2.3 Thermally Thin and Thermally Thick

A common engineering method in ignition problems is determining a solids ability to resist a temperature is whether a solid is thermally thin or thermally thick [8]. A solid that is thermally thin will have no temperature gradients within the solid. Thermally thick solids in comparison have a greater ability to resist a temperature rise resulting in temperature gradients through the solid. However, if exposed to a radiant heat flux for an extended time every solid can viewed as a thermally thin as no gradients will be present in the solid. The non-dimensional Biot number indicates whether a solid is considered thermally thick or thin.

$$Bi = \frac{hL}{k} \; (Equation \; 13)$$

where h is the convective heat transfer coefficient (W/m²K), k is the thermal conductivity of the solid (W/m·K) and L is the characteristic length (m).

Solids with Biot numbers <0.1 have small temperature gradients within the solid and are classified as thermally thin whilst Biot numbers >0.1 contain relatively larger temperature gradients and are considered thermally thick. The higher a materials thermal conductivity the more likely it is to be thermally thin. The same is true for the 'slimmer' the material is the more likely it is to be thermally thin. Materials with a thickness of less than 1mm can be treated as thermally thin [30].

2.4   Ignition

If a pilot ignition source (e.g., flame, spark) is present above the heated solid, after a certain time of exposure the temperature of the solid will cause a sufficient flow of volatiles/vapours to be within flammable limits and ignite [30]. There are two limits between which ignition can occur. These limits are known as the lower and upper flammability limits. At lower flammability limit the percentage of fuel within the air mixture above the surface is too low to facilitate ignition (i.e., fuel lean mixture) and at the upper flammability limit there is too much fuel within the air mixture (i.e., fuel rich mixture). After ignition occurs a diffusion flame will propagate through the regions in which a flammable mixture is present consuming the reactants.
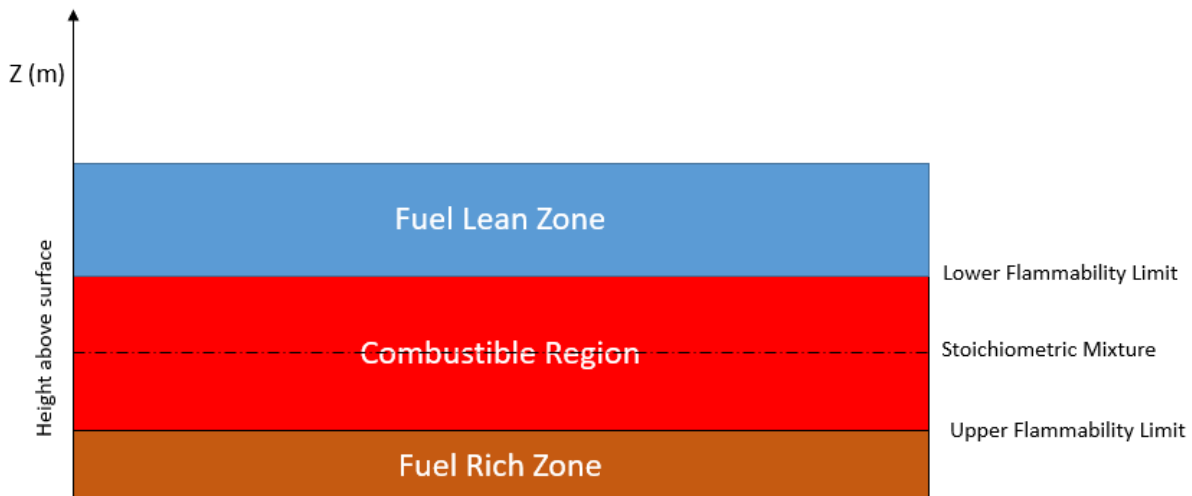
Figure 3 Flammable zones above the solid.

Analytical solutions have been derived to find approximate solution for t_{ig} and T_{ig} for thermally thick and thermally thin bodies when exposed to a heat flux and pilot ignition source. These solutions have been derived by considering an energy balance for a solid heated on one side. With the assumption that the solid is inert prior to t_p and that $t_{ig} = t_p$. The exact derivations can be found in an Introduction to Fire Dynamics by Douglas Drysdale and will not be discussed in detail here.

$$t_{ig,thick} \approx \frac{\pi}{4} k\rho c \frac{(T_{ig} - T_\infty)^2}{q''_r{}^2} \quad or \quad t_{ig,thin} \approx \rho c d \frac{(T_{ig} - T_\infty)}{q''_r} \; (Equation \; 14 \; \& \; 15)$$

where t_{ig} is time to ignition (s), ρ is the density of the material (kg/m³), k is the thermal conductivity of the solid (W/m·K), c is the thermal heat capacity (J/kg·K), L is the thickness of the material (m) q''_r is the incident heat flux (kW/m²), T_{ig} is the ignition temperature (K) and T_∞ is the ambient temperature (K).

2.5   Plume

Once a fuel source is ignited and sustained burning occurs a flame will form with a resulting fire plume [31]. A buoyant diffusion flame occurs whenever the fuel and oxygen are initially separated and will mix through diffusion with flaming only occurring if the mixtures are favourable for combustion (see section 2.3). If combustion occurs the heat produced will cause a temperature rise in the local gases, this temperature rise will decrease the density of the fluid in the vicinity of the reaction. As the density decreases the fluid will begin rise above the adjacent less dense gas resulting in an upward buoyant force as per the Archimedes principle. The buoyant force will contain any flames and soot and is commonly known as the fire or buoyant plume. As the hot air in the plume rises above the fire source cold air is entrained into the plume increasing the volume of the plume, this will cause a hot gas layer to form if the fire occurs within an enclosure. [7,30]

Fire plumes are commonly divided into three zones as shown by the diagram of the free burning or axisymmetric plume as shown in figure 1 below. There is a continuous flaming zone, an intermittent flaming zone and far field zone or buoyant plume zone where no flaming is evident.
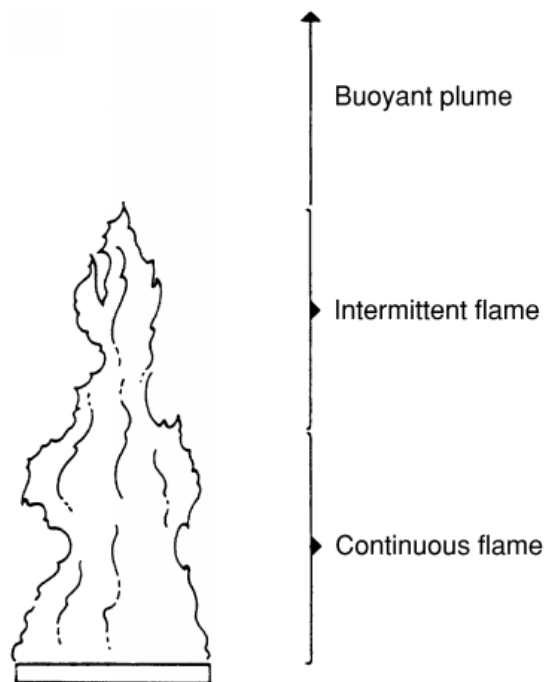
Figure 4 Zones of an axisymmetric buoyant plume. Figure reproduced from [7].

The highest temperatures in the plume occur along the centreline of the plume. In the continuous flame region, the temperatures are nearly constant, and it is often classified as the mean flame temperature. The centreline temperature of the plume decreases with height due to the increasing amount of air being entrained into the plume. Due to this entrainment of air the radius and mass flow rate of the plume increases with height. Most of the mass within the plume is due to the amount of entrained air. In larger diffusion flames turbulence will begin to

affect the structure of the plume/flame. The influence of the turbulence will cause the flame to oscillate which forms eddies/swirls to be manifest within the structure of the flame. [7]

2.6   Flame Spread over a surface

Flame spread can be viewed as a series of successive ignitions. If the initial ignition event results in a diffusion flame (see section 2.4), this diffusion flame will then heat the fuel adjacent to it pyrolyzing it producing further flammable vapours which can then subsequently ignite [32]. Just as in ignition, the rate of flame spread over a solid is dependent on a variety of variables such as the orientation, thickness, thermal inertia and other environmental effects. It is obvious that rate of spread will be dependent on whether the material can be considered 'thermally thick' or 'thermally thin' (see section 2.3). In the thermally thin case, there will be no temperature gradients within the solid thus the preheated material will reach its ignition temperature quicker when compared to a thermally thick case. In the thermally thick case the rate of spread will be independent of the thickness of the material a similar result was noticed [8] that as the thickness of a material is increased the rate of spread ultimately becomes independent.

There are two types of flame of surface flame spread that occur, these are concurrent flame spread and opposed flame spread. Concurrent flame spread is when the flow of air and the direction of the flame spread are in the same direction and opposed flow flame spread is when the entrained air and spread of flame occur in the opposite direction. For horizontal flame spread concurrent flame spread tends to happen when there is an imposed air flow whilst opposed flow flame spread is the way in which flame will horizontally spread in a quiescent environment [30].
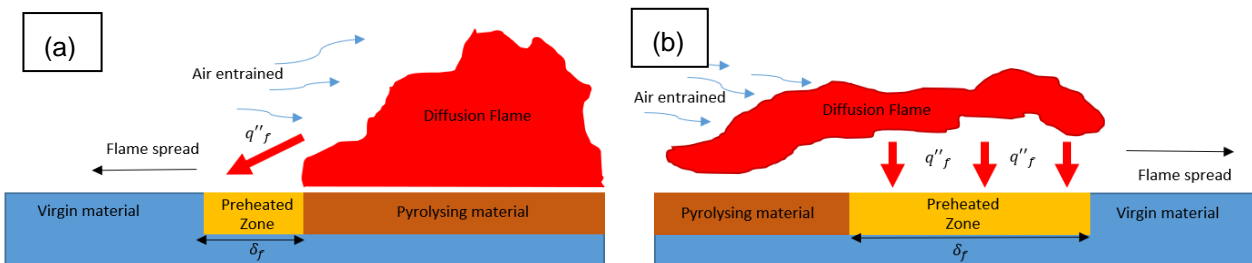
Figure 5 Schematic of a) opposed flow flame spread and b) concurrent flow flame spread.

As flame spread can be viewed as a series of ignitions [33] a simple indicative rate of flame spread can be calculated by dividing the preheated zone by the time to ignition as shown in equation 16 below.

$$v_p = \frac{\delta_f}{t_{ig}} \ (Equation \ 16)$$

where t_{ig} is the time to ignition (s) and δ_f is the preheated zone (m).

2.7   Influence of Corners on Flame Spread

Corner fires have been observed to be more intense than in axisymmetric plumes with the same heat release rate [10,34–36] and is why corner configuration as used to test wall linings

in Europe. In corner fires both mechanisms of flame spread occur concurrent for vertical flame spread and opposed for horizontal flame spread. The geometry of corner fires facilitates an increased rate of flame spread in comparison free of single wall bounded plumes. In corner fires the fire source is between two panels at 90° angles resulting in less entrainment of air into the as the entrainment is restricted to two sides.
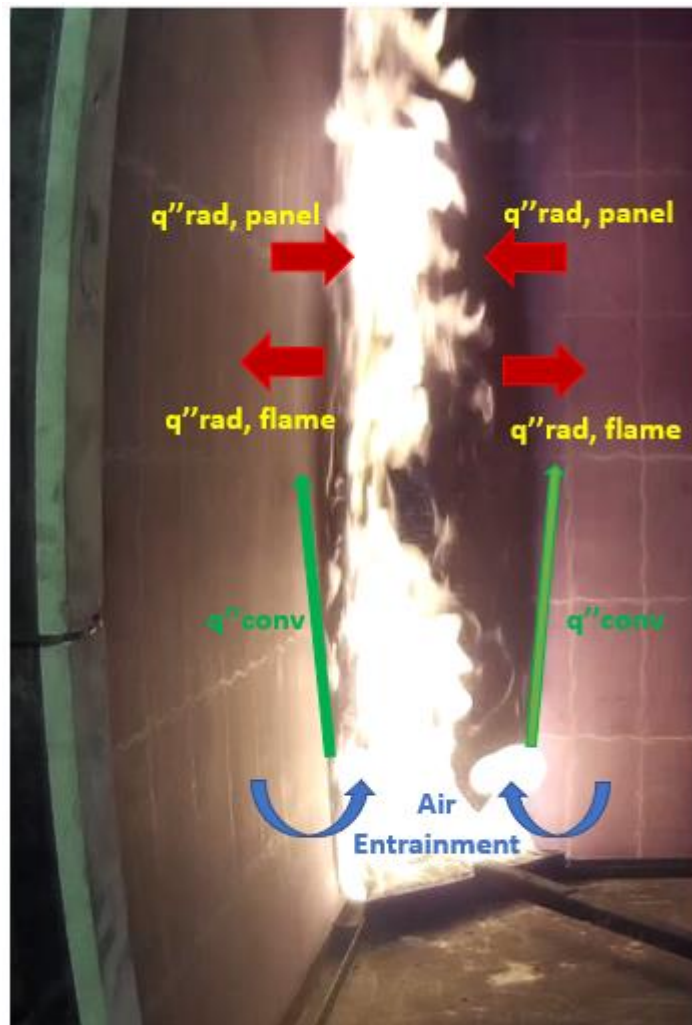
Figure 6 Corner fire example in the SBI test.

In corner fire scenarios the entrainment of air is approximately 40% of that which would occur in a free plume [37]. This reduced entrainment of air has the effect of increasing the temperature of the plume as the cooling effects of the air are reduced resulting in an increased heat flux from the flame, extending the preheated area and decreasing the time to ignition for the virgin material. This reduced entrainment will increase vertical flame spread as flame heights increase due to the gaseous fuel travelling further before combustion can occur.

In free burning plumes large amounts of radiation is lost to the surroundings, however in a corner scenario the panels will absorb some of these loses with a feedback mechanism developing due to the panels re-radiating heat increasing the total heat flux on the panels and thus extending pre-heated area.

3 FIRE MODELLING

Due to the inherent complexity of fire as discussed above practical all-encompassing mathematical models of fire are a recent development. To date there have been a variety of methods developed in order to predict the fire that attempt to incorporate the heat transfer, fluid dynamics, multi-phase flow and turbulent mixing of the fluids. The methods developed are there Zone Models and field models (CFD) including Reynolds Averaged Navier-Stokes (RANS), Large Eddy Simulations (LES) and Direct Numerical Simulations (DNS).

Zone Models have been developed by considering two separate homogenous volumes a hot upper layer and cool lower layer where the mass and energy balances are solved, additional empirical models are used to describe other aspects of the fire phenomena such as plumes, convective & radiative heat transfer and fuel pyrolysis. The other methods of simulating a fire are a lot more complex than in zone models as they use a set of partial differential equations asserting the conservation of mass, momentum and energy. When solved numerically these equations will produce predictions which vary in time of temperature, species concentration, velocities etc in the mesh of control volumes. [38]. These governing equations are displayed below:

Governing Equations

- *Conservation of mass:*

$$\frac{\partial \rho}{\partial t} + \frac{\partial \rho u_j}{\partial x_j} = 0 \ (Equation \ 17)$$

The conservation of mass simply states that mass is neither created nor destroyed but is conserved. In a fluid flow the change of density at a particular point is equal to the net mass flux across the boundary of a control volume which surrounds the point [39,40].

- *Conservation of momentum:*

$$\frac{\partial \rho u_i}{\partial t} + \frac{\partial \rho u_i u_j}{\partial x_j} = -\frac{\partial p}{\partial x_i} + \frac{\partial \sigma_{ij}}{\partial x_j} + \rho g, \qquad i = 1,2,3 \ (Equation \ 18)$$

The conservation of momentum states that the total momentum of a system is constant. The forces that drive the fluid are pressure gradient $\frac{\partial p}{\partial x_i}$, friction forces represented by the stress tensor σ_{ij} and the buoyancy force ρg [40]. The conservation of momentum has three equations for each velocity component u, v and w. The equations describing the conservation of momentum are often called the Navier-Stokes equations.

- Conservation of chemical species

$$\frac{\partial (\rho Y_i)}{\partial t} + \frac{\partial \rho u_j Y_i}{\partial x_j} = \rho D_i \frac{\partial Y_i}{\partial x_j} + \dot{\omega}_{Y_i}, \ i = 1, 2 \dots \ (Equation \ 19)$$

where Y_i is the species mass fraction, D_i is the mass diffusion coefficient and $\dot{\omega}_{Y_i}$ is the chemical reaction rate. Summation of all the transport equations for the chemical species results in the mass conservation equation.

- Energy Equation:

$$\frac{\partial \rho h_s}{\partial t} + \frac{\partial \rho h u_j}{\partial x_j} = \frac{Dp}{Dt} + \frac{\partial}{\partial x_j}(q_j) - \nabla . \dot{q}_r''' + \dot{q}''' (Equation \ 20)$$

The sensible enthalpy h_s at any given point in the fluid changes according to the net energy flux through the boundary like in the mass conservation equation. In contrast to mass conservation a variety other source terms have been introduced for combustion heat release rate $\dot{q}'''$, the pressure p, heat flux due to conduction q_j and the heat flux due to radiation $\dot{q}_r'''$.[39]

Equation of State:
The partial differential equations described above are dependent on the variables of density, velocity, enthalpy and pressure. To solve the system an equation of state is needed to relate pressure and enthalpy. In fire applications it is a sufficient assumption to consider a perfect gas which provides the following relationship relating pressure, density and temperature [17,40]:

$$p = \frac{\rho R T}{W} \ (Equation \ 21)$$

where p is the pressure (N/m^2), R is the universal constant (J/Kmol), T is the temperature (K) and W is the average molecular weight of the gases (g/mol). From the idea gas law, the sensible enthalpy can be calculated as it is a function of the specific heat and temperature of the fluid:

$$h = \int_{T_0}^{T} c_p \ \partial T \ (Equation \ 22)$$

where c_p is the specific heat (J/kgK) and T$_0$ is a reference temperature (K)

The governing equations can further be simplified as thermally driven flows from fire are significantly slower than the speed of sound. In CFD literature this is referred to as a low-Mach number flows, this number represents the ratio of flow speed to the speed of sound in the fluid. In low-Mach number flows (≤0.3) it is no longer needed to account for pressure fluctuations that will propagate through the fluid as it approaches the speed of sound. The pressure can then be assumed to be either constant or a time varying average allowing temperature to be calculated directly from the density. [40].

3.1   Computational Fluid Dynamics

In CFD simulations the governing equation are solved numerically by dividing the physical geometry, where the fire is to be simulated, into a number of cells. These cells can be a variety of shapes with scalar quantities such as the density and temperature defined at the cell centre, velocity components are calculated at the cell faces and the vorticity components are estimated at the edges.
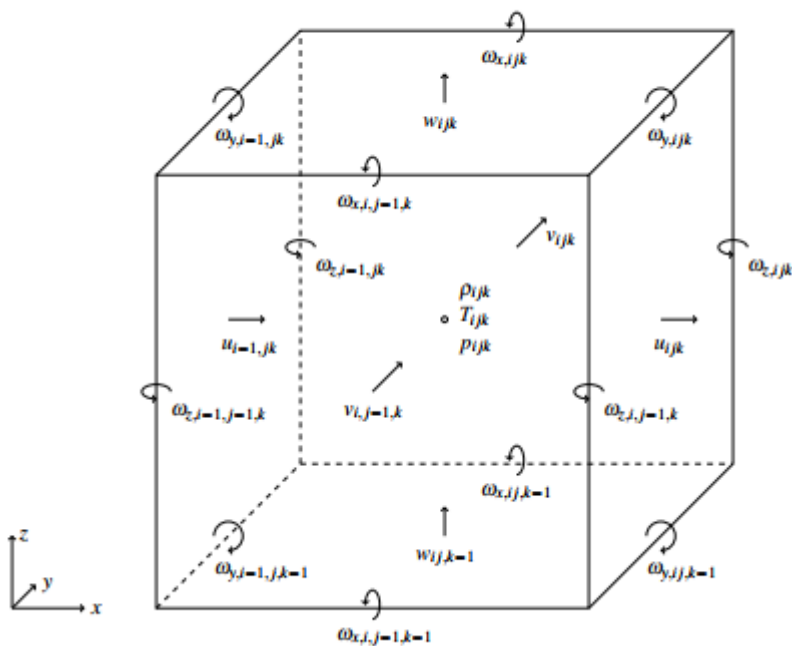
Figure 7 Example of a rectangular parallelepiped cell. Figure reproduced from [39].

DNS simulations aim to solve the exact solution to the conservation equations and is extremely computationally expensive requiring cell sizes in the order magnitude off less than 1 mm. RANS models, on the other hand, are comparatively computationally cheap and provide time-averaged solutions of the general equations. These models require the introduction of large eddy transport coefficients to describe the fluxes of mass, momentum and energy that are unresolved.

LES is derived in a similar manned to RANS, as opposed to adopting a time averaged form of the conservation equations in LES adopts a spatial filtering of conservation equations. LES attempt to resolve the flow field as much as possible on the numerical grid. Eddies or swirls within the flow can span multiple grid cells and account for most of the mixing and are large enough to be calculated to a reasonable accuracy, the smaller eddies(sub grid scale) are either crudely accounted for by sub grid modelling or are discounted all together. In fire scenarios the dominant mode for the transport of heat and products is via the convection process, which is a relatively large-scale phenomenon in comparison to the diffusion process. The diffusion processes include viscous effects on the flow, thermal conductivity of the fluid, mass diffusivity and production from pyrolysis play a significant role around the fire and near the surface of solids. Calculating both the large and small-scale processes, as is done in DNS, is extremely computationally expensive and, due to this, models are employed to describe the sub-grid scale phenomena (smaller than the cell size). LES will resolve the mean values of mass, momentum and energy explicitly while modelling for the effects of the subgrid scale transport and chemistry have on the mean values.

A low pass filter parameterized by the width Δ is applied to the governing equations for mass, momentum and energy. Δ is typically taken as $\Delta=(\Delta x \Delta y \Delta z)^{1/3}$ where $\Delta x, \Delta y$ and Δz are the sides of a grid cell. An example from the application of the filtering method to the momentum equation which is done in FDS is shown overleaf:

$$\frac{\partial}{\partial t}(\overline{\rho u_i}) + \frac{\partial}{\partial x_j}(\overline{\rho u_i u_j}) = -\frac{\partial \bar{p}}{\partial x_i} - \frac{\partial \overline{\sigma_{ij}}}{\partial x_j} + \bar{\rho} g \quad (Equation\ 23)$$

There is no way to compute the cell mean value of $\overline{\rho u_i u_j}$ and as such the variables must be decomposed in which result in a closure problem. When decomposing the scalar quantities, the instantaneous values are broken up into grid resolved components and a subgrid scale component:

$$\phi(x,y,t,z) = \underbrace{\bar{\phi}(x,y,t,z)}_{\substack{Grid\ Resolved \\ Component}} + \underbrace{\phi'(x,y,t,z)}_{\substack{Subgrid-Scale \\ Component}} \quad (Equation\ 24)$$

where

$$\bar{\phi}(x,y,z,t) = \frac{1}{V_c} \int_{x+\partial x/2}^{x+\partial x/2} \int_{y+\partial y/2}^{x+\partial y/2} \int_{z+\partial z/2}^{z+\partial z/2} \phi(x',y',z',t)\,dx'dy'dz' (Equation\ 25)$$

The next step is to apply the Favre filter which results in:

$$\frac{\partial}{\partial t}(\bar{\rho}\tilde{u}_i) + \frac{\partial}{\partial x_j}(\bar{\rho}\widetilde{u_i u_j}) = -\frac{\partial \bar{p}}{\partial x_i} + \frac{\partial \overline{\sigma_{ij}}}{\partial x_j} + \bar{\rho} g \quad (Equation\ 26)$$

Provided that there is a solution for $\bar{p}$ the term $\bar{\rho}\widetilde{u_i u_j}$ is now separable,although the term $\widetilde{u_i u_j}$ still cannot be calculated on the computational grid. To get by this, the subgrid-scale stress is defined as:

$$\sigma_{ij}^{SGS} = \bar{\rho}(\widetilde{u_i u_j} - \tilde{u}_i \tilde{u}_j) \quad (Equation\ 27)$$

thus

$$\bar{\rho}\widetilde{u_i u_j} = \sigma_{ij}^{SGS} - \bar{\rho}\tilde{u}_i \tilde{u}_j \quad (Equation\ 28)$$

Substituting equation 28 into 26:

$$\frac{\partial}{\partial t}(\bar{\rho}\tilde{u}_i) + \frac{\partial}{\partial x_j}(\bar{\rho}\tilde{u}_i \tilde{u}_j) = -\frac{\partial \bar{p}}{\partial x_i} - \frac{\partial \overline{\sigma_{ij}}}{\partial x_j} - \frac{\partial \sigma_{ij}^{SGS}}{\partial x_j} + \bar{\rho} g \quad (Equation\ 29)$$

This is now an LES momentum equation in which all the variable can be calculated provided there is a suitable closure for the subgrid scale stress σ_{ij}^{SGS}. Further modifications can be made to the equation prior to running a simulation in FDS. The subgrid scale stress can be decomposed with Newton's law of viscosity being applied for the deviatoric part of the viscous stress:

$$\sigma_{ij}^{dev} = \overline{\sigma_{ij}} + \sigma_{ij}^{SGS} - \frac{1}{3}\sigma_{kk}^{SGS}\delta_{ij} = -2(\mu + \mu_t)(\tilde{S}_{ij} - \frac{1}{3}(\nabla\bar{u})\delta_{ij}) \quad (Equation\ 30)$$

where μ_t is the turbulent viscosity and δ_{ij} is the Kronecker delta defined as:

$$\delta_{ij} = \begin{cases} 1 & i = k \\ 0 & i \neq j \end{cases} \quad (Equation\ 31)$$

The isotropic part of the subgrid scale stress will be absorbed by the pressure term for low-Mach flows. The subgrid kinetic energy is defined as half the trace of the SGS stress as:

$$k_{SGS} = \frac{1}{2} \sigma_{kk}^{SGS} \ (Equation \ 32)$$

From this, the modified filtered pressure can be determined as:

$$\bar{p} = \bar{p} + \frac{2}{3} k_{SGS} \quad (Equation \ 33)$$

Substituting equation 33 into equation 29:

$$\frac{\partial}{\partial t}(\bar{\rho}\widetilde{u_i}) + \frac{\partial}{\partial x_j}(\bar{\rho}\widetilde{u_i}\widetilde{u_j}) = -\frac{\partial \bar{p}}{\partial x_i} - \frac{\partial \sigma_{ij}^{dev}}{\partial x_j} + \bar{\rho}g \quad (Equation \ 34)$$

It should be noted that the turbulent viscosity μ_t will need to be modelled. Details on solving turbulent viscosity for the above equation along with the source terms in energy equation are discussed in chapter 5.

3.2   Grid Size

The accuracy of the simulation tends to depend on the number of cells in the simulation, the higher the number of cells then generally the more accurate the simulation in other words the smaller the cell size the more accurate the simulation. In buoyant plumes a rule of thumb has been developed to determine how well the flow field is resolved based around R* and the characteristic fire diameter D* [37,41]:

$$R^* = \frac{max(\Delta x, \Delta y, \Delta z)}{D^*} \ (Equation \ 35)$$

where

$$D^* = \left(\frac{\dot{Q}}{\rho_\infty T_\infty c_p \sqrt{g}}\right)^{2/5} \ (Equation \ 36)$$

where $\Delta x, \Delta y, \Delta z$ is the size of the cell in the x, y or z direction, $\dot{Q}$ is the heat release rate (kW), ρ_∞ is the ambient density of air (kg/m^3), T_∞ is the ambient temperature of the air (K), c_p is the specific heat of air (kJ/kg·K), and g is the acceleration due to gravity (m/s^2).

Previous studies show that R* values of about 0.1 or smaller are sufficient to accurately predict the dynamics of free plumes [37,41,42] . It should however be noted that for wall flows the resolution is not as simple due to the boundary layer effects. It has been observed that to resolve wall bounded flows that grid sizes of approximately 3 mm are required. Thus, the convective heat transfer of these flows tends to be modelled for engineering applications.

4 SBI CASE

The Single Burning item test is the testing procedure used withing the European Union to classify the response of lining materials to fire. It is an intermediary test regime between bench scale tests such as the cone calorimeter or fire propagation apparatus tests and large-scale fire tests such as the ISO room corner test.

In the SBI test two panels are placed perpendicular to each other which are mounted on an SBI testing trolley. There is a long panel measuring 1.5m high and 1.0m wide and a short panel with a height of 1.5m and a width 1.0m the panels, prior to testing the panels have been conditioned at 21°C and 50% relative humidity. The test involves using an isosceles triangular burner with side lengths of 0.25m which is placed at a distance of 0.04m from the panels. The fuel source burner is propane with the HRR from the burner being adjusted so that it will take approximately 30s to achieve HRR of 30kW.
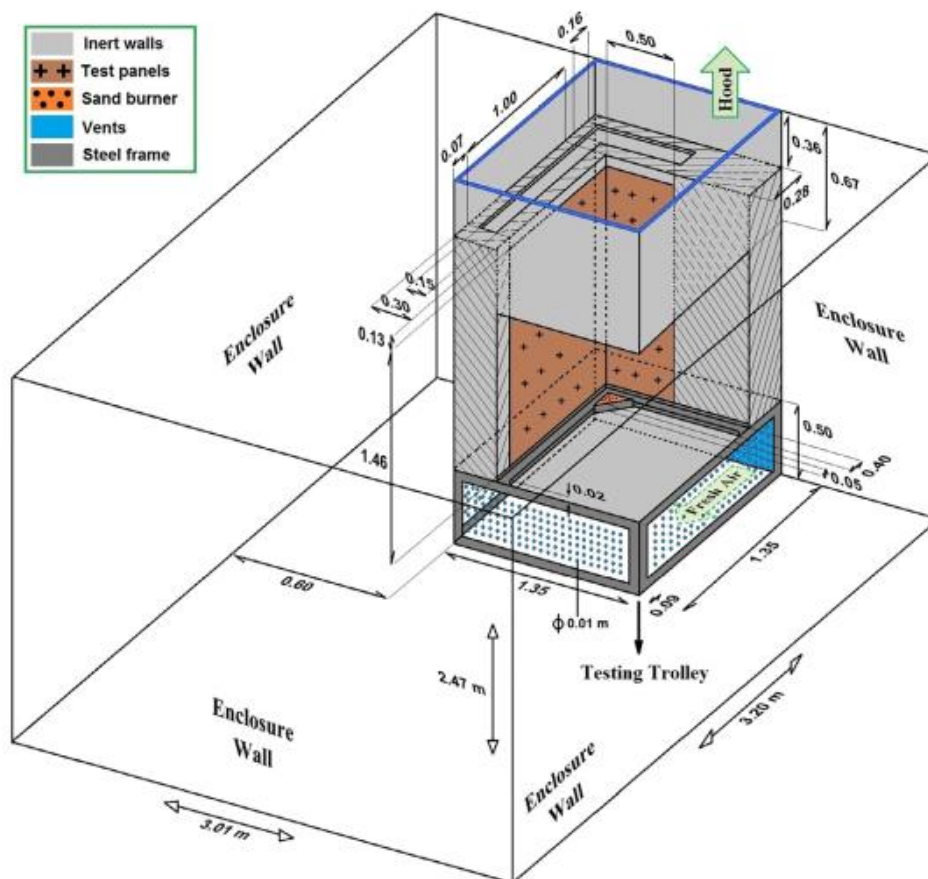
Figure 8 Geometry of the SBI testing enclosure (Reproduced from the work of Zeinali [13]).

Two opening are provided in the enclosure a vent at the bottom of the backside of the enclosure of the trolley measuring 1.16m x 0.32 m which provides fresh air into the enclosure. The hood at the top extracts the gases and the smoke.

4.1 Experimental work conducted by Zeinali ([12,13])

Zeinali carried experimental and numerical work as part of a PHD thesis on flame spread in a corner configuration. The work conducted experiments on inert Calcium silicate panels, Medium-Density Fibre Board and Plywood panels. Considered within these tests was the influence of a single flammable panel with an inert board and with both flammable panels in a corner configuration.

In the tests a variety of parameters were measured to assess the impact of the fire on the panels. The total HRR and smoke production rates were measured with the flame spread on each panel being monitored using video cameras. The through thickness panel temperatures were measure using type k thermocouples with diameters of 0.0005m at distinct locations as shown below in figure 9. The vertical flame heights were measure by the use puffing frequency and total heat flux was measured by Schmidt-Boelter heat flux sensors.
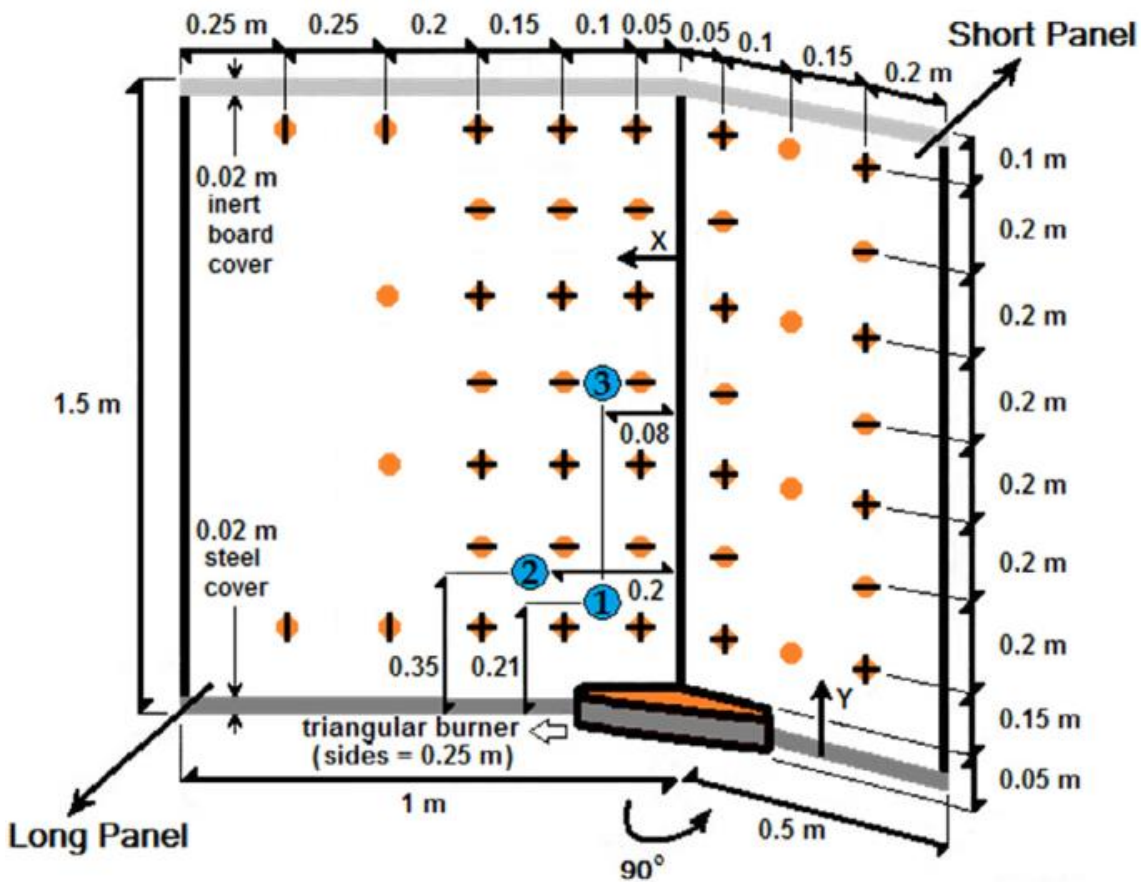
Figure 9 Layout of measurements made on the SBI test. The orange circle indicates that the temperatures at 0.001m depth are only measured, orange circle with vertical line indicates that the temperatures at 0.001m depth and at the backside are measured, orange circle with horizontal line indicates that the temperatures at depths 0.001m and 0.002m are measured, orange circle with a cross indicates that the temperatures at depths 0.001m, 0.002m and the backside are measured whilst the blue circles indicate where the total heat fluxes are measure. The figure has been reproduced from [13].

Three tests were carried out for the plywood panels, whilst the experimental results were not exactly the same, they did have reasonable repeatability adhering to the same trends.

The total HRR from the three experiments is shown below in figure 10. The total HRR accounts for both the influence of the triangle burner and the combustible walls where:

$$\dot{Q}_{total} = \dot{Q}_{Burner} + \dot{Q}_{Panels} \ (Equation \ 37)$$

where $\dot{Q}$ is the HRR (kW)

In the plywood corner tests two distinct peaks where observed, the first is mainly due to vertical flame spread which occurs at times between 100-125s with the second peak being mainly associated with horizontal flame spread occurring at approximately 270-300s. After the second peak the total HRR begins to decrease until a 'quasi' steady state is reached, in two of the tests experiment 1 and experiment 3 the fire penetrates the corner at 1035 and 1071s respectively resulting in a rapid increase in the HRR.
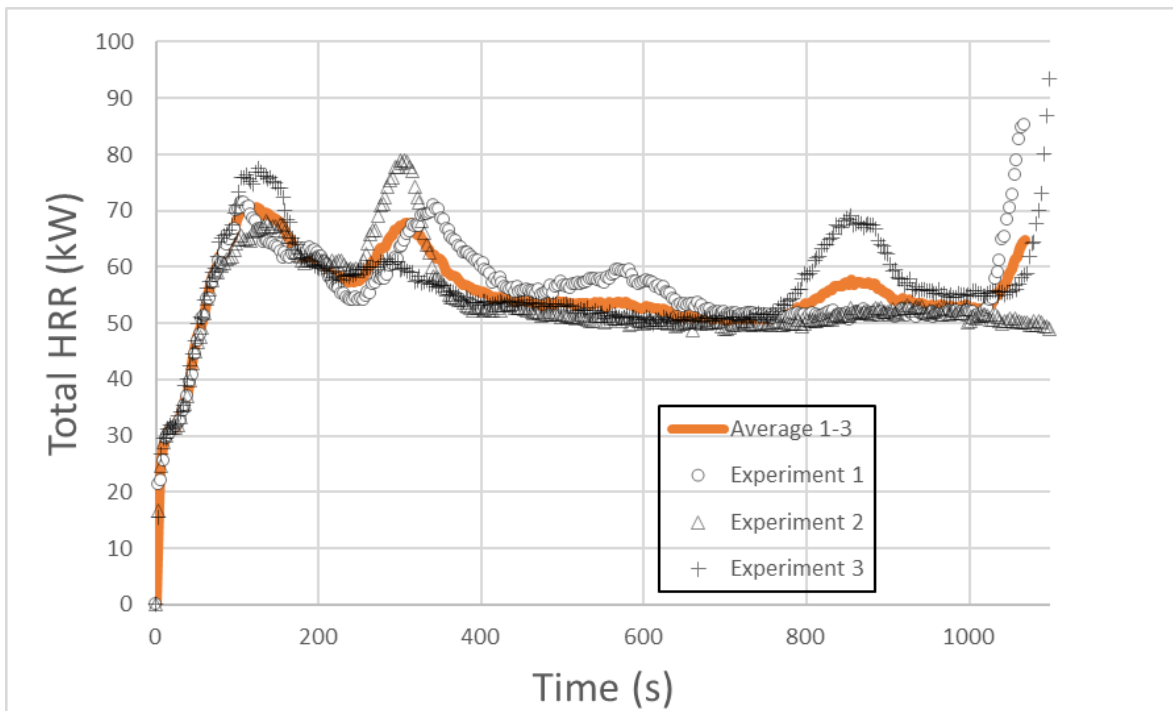
Figure 10 Total HRR for the three plywood experiments

5   NUMERICAL SIMULATION

The simulations performed in this study were carried by using FDS v6.7.0 developed by NIST [11,41–43]. FDS is capable of DNS and LES simulations with an emphasis on smoke and heat transfer. The package numerically solves the Navier-Stokes equations considering a low-Mach approximation with an emphasis on fire related flows. The package has been subject to extensive validation studies for a variety of different fire related problems [44].

The simulations attempted to replicate the SBI corner fire test as described in chapter 4. The geometry of the computational domain is shown in figure 11. The dimensions of the computational domain are 1.2m x 1.32m x 2.4m. this computational domain is a simplified version of the geometry of the SBI test including only the room where the burner and panels are located. This is in line with previous numerical studies of the SBI test [15,16], however this study will extend the domain to attempt to model the heat losses to the back of the panes. The extended geometry of the enclosure is not included to reduce the computation time. There has been a previous study where the entire geometry was included which resulted in only 'slightly' better results [23].
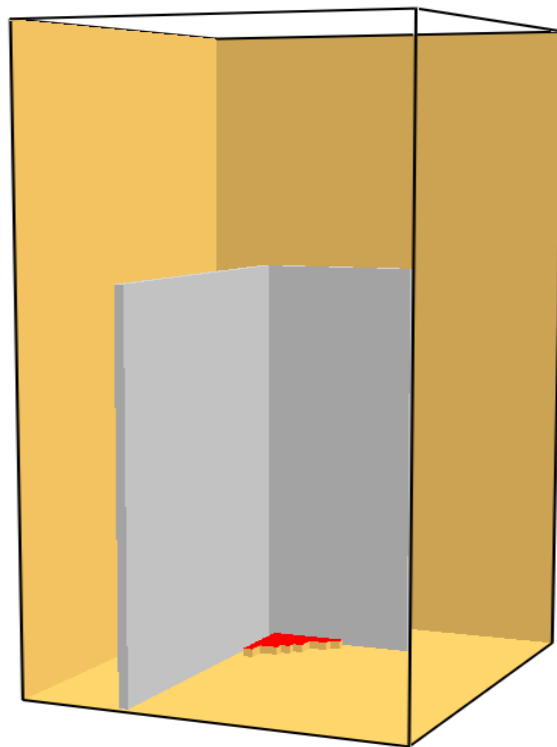
Figure 11 Computational Domain as observed through Smokeview.

5.1   Simulation Details

The total time of the simulation is 700s as is shown in the experimental results after 600s a quasi-steady state is achieved, at later times in two of the tests the fire penetrates the corner. There is an open boundary at the top and sides opposite the panels, the open boundaries opposite the panel represent the opening of the room in the SBI test. Typical ambient conditions exist beyond the boundaries with the temperature being 20ºC and the pressure being 101325 PA. As only rectilinear cell shapes are allowed in FDS the triangle burner has been approximated as series of rectangles.

There are three cubic cell sizes used in this analysis with dimensions of 4cm, 3cm and 2cm. The total number of cells for the gas phase of each simulation is shown in Table 1 below. A sample FDS file of the simulation is also presented in the appendix.

Table 1. Total number of cells for given cell size

Cell size (cm)	Total no. of Cells
4	59, 400
3	140,800
2	613,800

5.2 Thermal Physical Properties

The thermal physical properties of the calcium silicate and plywood boards are displayed below and have been reproduced from the work of Zeinal [12]. The model effective properties of the plywood were obtained by the inverse modelling of multiple FPA tests in a nitrogen environment using the 1D pyrolysis model in FireFoam CFD package [12]. Whilst FDS is a different CFD packages it also employs a 1D heat conduction and pyrolysis model. This study will demonstrate efficacy or lack thereof of using these model effective properties

Table 2. Model-effective material properties

Property	Calcium Silicate	Plywood
L, Thickness (m)	0.0123	0.017
k_v, Thermal conductivity of virgin material (W/mk)	0.17	0.12[a]
ρ_v, Density of virgin material (kg/m^3)	1005	560[a]
C_v Specific heat capacity of virgin material (J/kgK)	920	1329.56[a]
Net lower heating value of virgin material (MJ/kg)	-	19.6[b]
Heat of combustion of pyrolyzate^a (MJ/kg)		10.17[c]
x_c Char fraction	-	0.15[a]
k_c, Thermal conductivity of char (W/mK)	-	0.19[a]
ρ_c, Density of char (kg/m^3)	-	82.03[a]
C_c Specific heat capacity of char (J/kgK)	-	1450[a]
A, Pre-Exponential factor (s^{-1})	-	6.3 x 10^{4}[a]
E, Activation Energy (J/mol)	-	8.01 x 10^{4}[a]
Heat of Reaction (J/kg)	-	-2.15 x 10^{5}[d]

a) Model effective property developed through inverse modelling of FPA tests in Nitrogen

b) Determined through bomb calorimeter tests.
c) Effective heat of combustion of pyrolysate. Determined through an FPA test for the initial flaming period prior to any significant char format.
d) Negative value indicates that it is an exothermic reaction

5.3   Turbulence modelling

In this study, the default Deardorff turbulence model has been used to close the subgrid scale momentum and scalar flux terms as identified in section 3. The subgrid scale viscosity and kinetic energy can be modelled by the following:

$$\mu_{sgs} = \rho C_v \Delta \sqrt{k_{sgs}} \; ; \quad k_{sgs} = \frac{1}{2} ((\bar{u} - \hat{u})^2 + (\bar{v} - \hat{v})^2 + (\bar{w} - \hat{w})^2) \; (Equation \; 38)$$

where ρ density of the gas, Δ is the filter width, $\bar{u}$ is the average value of u at the grid cell centre and $\hat{u}$ is the weighted average of u over the adjacent cells.

$$\bar{u}_{ijk} = \frac{\bar{u}_{ijk} + \bar{u}_{i-1jk}}{2} \; ; \; \hat{u}_{ijk} = \frac{\bar{u}_{ijk}}{2} + \frac{\bar{u}_{i-1jk} \; \bar{u}_{i+1jk}}{4} \; (Equation \; 39)$$

The terms v and w are defined similarly. In this study the model constant will be kept at the default setting of C_v = 0.1 [42]. A sensitivity study was also carried out using the WALE turbulence available in FDS, however, no significant differences were observed. These simulations are included in the appendix.

5.4   Combustion modelling

The combustion model used for this study is the mixing-controlled, infinitely fast reaction of lumped species. The lumped species transport equations are only solved for the products, air and the fuel species. Considering lumped species significantly reduces the computational demand as only three transports equations will need solved as opposed to solving for all the major reactants and products of combustion. In an infinitely-fast reaction the reactant species within a cell are converted to the product species. The rate at which this reaction occurs is determined by the characteristic mixing time. Where the characteristic mixing time scale is calculated as:

$$\tau_{mix} = \max{(\tau_{chem}, \min(\tau_d, \tau_u, \tau_g, \tau_{flame})} \; (Equation \; 40)$$

where

$$\tau_d = \frac{\Delta^2}{Df} \; (Equation \; 41)$$

$$\tau_u = \frac{C_u \Delta}{\sqrt{(2/3) \; k_{sgs}}} \; (Equation \; 42)$$

$$\tau_g = \sqrt{\frac{2\Delta}{g}} \; (Equation \; 43)$$

where Δ is the filter width, C_u is the advective time scale constant = 0.4, Df is the diffusivity of the fuel species and g is the acceleration due to gravity (9.8 m/s²). The time scale which characterises the mixing time scales are dependent on the flow condition. In scenarios were gravity is weak τ_g will not affect the reaction time prior to the time scale of τ_{flame} being reached. In highly turbulent flows the time scale of τ_u decreases.

The heat release rate per unit volume can thus defined by summing the lumped species mass production rates time their respective heats of formation as:

$$\dot{q}''' = -\sum_a \dot{m}_a''' \Delta h_{f,\alpha} \; (Equation \; 44)$$

In the default infinitely fast combustion model there is only one gas phase reaction of fuel and oxygen determined by the global reaction. In this study the global reaction is for propane (C_3H_8). This is a computationally efficient method of modelling the combustion process as it allows for multiple solid phase reactions with only one gas phase reaction. To ensure that the correct HRR is attained, the mass flow from the solid will be adjusted to produce the correct amount established by the heat of combustion (energy released per unit mass of fuel gas that mixes with oxygen and combusts) of the solid.

5.5 Conduction modelling

This study utilizes the default one dimensional heat conduction equation in which heat transfer is assumed only in the direction normal to the surface.

$$\rho_s c_s \frac{\partial T_s}{\partial t} = \frac{\partial}{\partial x}\left(k_s \frac{\partial T_s}{\partial x}\right) + \dot{q}_s''' \; (Equation \; 45)$$

The source term $\dot{q}_s'''$ consists of chemical reaction and radiative absorption

$$\dot{q}_s''' = \dot{q}_{s,c}''' + \dot{q}_{s,r}''' \; (Equation \; 46)$$

where $\dot{q}_{s,c}'''$ is the heat loss rate due to pyrolysis (see below) and $\dot{q}_{s,r}'''$ is the radiative absorption and emission in depth.

The boundary condition at the surface is given by:

$$-k_s \frac{\partial T_s}{\partial x}(0,t) = \dot{q}_c'' + \dot{q}_r'' \; (Equation \; 47)$$

where $\dot{q}_c''$ is the convective heat flux and $\dot{q}_r''$ is the radiative heat flux. Equation 45 above is discretised with the size of the cell closest to the boundary equal to:

$$x = \sqrt{\frac{t_o k_s}{\rho_s c_s}} \; (Equation \; 48)$$

A Crank-Nicolson scheme is used to calculate the temperature of each cell at each time step[41]. As heat conduction and pyrolysis is a crucial aspect of this study each of the discretization's cells will be off equal length as the first cell this done by setting

STRETCH_FACTOR=1 on the SURF line. In the plywood scenario a total of 42 nodes will be used within the panel.

The default backside boundary condition will be applied in this study. As the thickness of the panel in all the cases is less than 1 mesh cell thick the heat transfer at the backside will be calculated similarly to equation 47 where

$$k_s \frac{\partial T_s}{\partial x}(0,t) = -(\dot{q}_c'' + \dot{q}_r'') \ (Equation \ 49)$$

5.6   Pyrolysis modelling

The source term in the heat conduction equation 45 will be discussed in this section. As deliberated in section 2.2, solids can undergo several reactions with each one potentially producing a solid residue and gaseous fuel. The pyrolysis model in this simulation is a simple one step reaction in which the virgin fuel reacts and converts the solid into fuel for the gas phase combustion and char in line with other numerical studies [12,23,45].

$$Virgin \rightarrow (1 - x_c)Fuel + x_c Char \ (Equation \ 50)$$

where x_c is the char yield.

The general equation for the evolution of a material undergoing one or more reactions:

$$\frac{dY_{s,a}}{dt} = -\sum_{B=1}^{N_{r,a}} r_{a,b} + S_a \ ; \ Y_{s,a} = \left(\frac{\rho_{s,a}}{\rho_s(0)}\right) (Equation \ 51)$$

The equation describes how the density of a material or component *i* evolves with time when undergoing a reaction, $N_{r,a}$ is the number of reactions for the material while $r_{a,b}$ defines the rate of reaction at the temperature T_s, calculated as:

$$r_{a,b} = \left(A_{ab} Y_{s,a}^{n_{s,ab}} \exp\left(-\frac{E_{ab}}{RT_s}\right)\right) (X_{O_2}^{n_{O_2,a,b}}) \ (Equation \ 52)$$

The second term S_a in equation 51 represents the production rate of the component due to the reaction of another component, $\rho_s(0)$ is the initial density of the solid, $\rho_{s,a}$ is the density after the reaction, A is the pre-exponential factor (s^{-1}) and E is the activation energy (J/mol). Values of A and E can be determined through thermogravimetric analysis, however the values are not available for most materials. The values of A and E used for the reaction in this simulation are shown in table 2. Equations 51 + 52 describe the rate at which a reaction occurs however solid phase reactions can either be endothermic of exothermic. Endothermic reactions are reactions that require energy and exothermic reactions produce energy or take it out from the system. The heat of reaction for wood species can be either endothermic of exothermic with endothermic with values up to 370 kJ/kg and exothermic values up to -1700 kJ/kg [46]. Thus, the source term $\dot{q}_{s,c}'''$ can be calculated as:

$$\dot{q}_{s,c}''' = -\rho_v \left(A_{ab} Y_{s,a}^{n_{s,ab}} \exp\left(-\frac{E_{ab}}{RT_s}\right)\right) (X_{O_2}^{n_{O_2,a,b}}) H_p \ (Equation \ 52)$$

where H_p is the heat of reaction (kJ/kg).

In the simulations once the reaction occurs 15% of the plywood will convert to char with the remaining 85% being converted into pyrolysate for the gas phase combustion. As outlined in section 2.2 the char can then further decompose producing more pyrolysate and leaving an inert residue (ash). Due to the obvious difficulties in quantifying the important variables in a char reaction such as the heat of reaction and values for A and E, it will be attempted to model the influence of char reaction on the heat release rate through the effective heat of combustion. The total effective heat of combustion can be viewed as having two separate contributing factors the heat released due to the pyrolysate and the heat released due to char oxidation.

$$\Delta H_{tot} = (1 - x_c)\Delta H_{pyrol} + x_c * \Delta H_{c,char} \ (Equation \ 53)$$

where ΔH_{tot} is the effective heat of combustion (MJ/kg), x_c is the char fraction ΔH_{pyrol} is the heat released due to the pyrolysate (MJ/kg) and $\Delta H_{c,char}$ is the heat of combustion of char (MJ/kg).

The effective heat of combustion for the plywood sample was determined from the lower heating value provided in table 2 assuming a combustion efficiency 0.7 for conifer wood products [47]. This results in an effective heat of combustion of 13.72 MJ/kg.

5.7   Radiation modelling

The net contribution due to thermal radiation in the energy equation is defined as:

$$\dot{q}_r''' \equiv -\nabla.\dot{q}_r''(x) = \kappa(x)[U(x) - 4\pi.I_b(x)] \ ; \ U(x) = \int_{4\pi} I(x,s')ds' \ (Equation \ 54)$$

where $\kappa(x)$ is the absorption coeffiecient, $I_b(x)$ is the source term and $I(x,s)$ is the solution to the radiation transport equation for a non scattereing gray gas:

$$s.\nabla I(x,s) = \kappa(x) [I_b(x) - I(x,s)] \ (Equation \ 55)$$

In reality, the spectral dependence on $\kappa(x)$, I, I_b cannot be resolved accurately. The mean absorption coefficient κ is a function of the temperature and species composition this value is obtained via a narrow-band model RADCAL. Due to the limited resolution afforded by the numerical grid the source term I_b requires special treatment as the flame sheet is often not accurately resolved. Consequently, the source term is only approximated within cells where fuel and oxygen react elsewhere the subgrid temperature field is homogenous and the source term can be computed directly:

$$\kappa I_b = \begin{cases} \kappa\sigma T^4/\pi \ Outside \ flame \ zone, \ q'''\dot{} = 0 \\ C\kappa\sigma T^4/\pi \ Inside \ flame \ zone, \ q'''\dot{} > 0 \end{cases} \ (Equation \ 56)$$

where the constant C is computed each time step so that the volume integral of equation 54 over the entire flaming region is approximately equal to the volume integral of $x_r q'''$ over that same region. The radiative fraction x_r is dependent on a variety of variables such as fire size, flame temperature along with the composition of fuel and combustion products. As the flame sheet will not be well resolved in coarse grids, the radiation emitted will not be calculated directly from the temperature due the T^4 dependence of radiation. To compensate for this inaccuracy every cell which is cut by the flame sheet radiates the fraction of chemical energy being released into it. Unfortunately, there is no data available on the radiative fraction of

plywood products however there are results for pine of which plywood is commonly made from. Pine has a radiative fraction of approximately 0.3 [48] with propane also having a radiative fraction of 0.3 [44]. As such the global radiative fraction is specified as 0.3 for the study that is that 30% of the total combustion energy will be released as thermal radiation. The radiation equation is then solved using the Finite Volume Method using the default of 104 discrete angles which are updated over multiple time steps.

5.8 Convective heat transfer modelling

It has been suggested that for turbulent flows near the wall cell sizes in the magnitude of millimetres [17–19], will be required to accurately resolve the change from molecular to turbulent transport near the walls along with the transport of heat near the wall for the calculation of the convective heat transfer. As such empirical and wall models will be used to calculate the convective heat transfer. This work will investigate the influence that the convective heat flux models have on the development and spread of fire on the panels. As shown in equation 5 the convective heat transfer is caused by the bulk motion of fluid and directly correlated to the temperature difference between the gas and the wall. Near the wall in turbulent flows there are sharp temperature gradients within the thermal boundary layer. In the simulations the temperature of the gas will be taken as the mean temperature at the centre of the cell beside the wall.

There are two methods available in FDS to model the convective heat transfer $\dot{q}_c''$ towards the solid which are discussed below. It is relevant to note that these models were developed by observing flow over inert bodies, inaccuracies are likely to develop for solids where pyrolysis occurs as mass is transported to the surface influencing the flow – the blowing effect.

It was attempted to conduct a DNS approach of FDS on the coarse grids however due to the coarse grid sizes nonsensical results were achieved as shown in the appendix.

4.3.2 Empirical Model (Default)
The empirical model is the default convective heat transfer model for FDS simulations. In this model the convective heat transfer is determined through a combination of natural and forced convection correlations:

$$\dot{q}_c'' = h(T_w - T_g) \ ; \ h = \max\left[C \left|T_g - T_w\right|^{\frac{1}{3}} \ , \frac{k}{L} Nu \ , \frac{k}{\frac{\partial n}{2}}\right] \ (Equation \ 57)$$

where C is an empirical coefficient for natural convection, L is the characteristic length related to the size of the physical obstruction and k is the thermal conductivity of the gas. Nu depends on the geometric and flow characteristics and is related to both the Prandtl and Reynolds numbers as discussed in section 2.1.2.

$$Nu = C1 + C2Re^n \Pr^m \ ; \ Re = \frac{\rho|\boldsymbol{u}|L}{\mu} \ ; \Pr = 0.7 \ (Equation \ 58)$$

Built into FDS are default value different surfaces for example the default values for planar surfaces are $C_1 = 0$, $C_2 = 0.037$, n = 0.8, m = 0.33 and L = 1m. These values can be changed for any given scenario. Correlations for different geometric shapes can be found in a variety of fluid dynamics or fire related textbooks. In this this study the default values will not be adjusted.

4.3.3 Near-wall model (WM)

The near wall model will attempt to model the sudden change from molecular to turbulent transport close to the walls by using algebraic formulations. This is achieved without resolving the smallest length scales [42] as required in wall resolved flows. The wall model is based on the concept that shear at the wall is zero (no slip boundary condition) which allows the non-dimensional velocity to be defined as a function of the non-dimensional length scale. The non-dimensional temperature can thus be defined by analogy with the non-dimensional velocity. Subsequently the non-dimensional temperature is defined as:

$$T^+ = \frac{T_g - T_w}{T\tau} \quad (Equation\ 59)$$

where Tg is the first off-wall gas phase cell temperature. The non-dimensional temperature from the wall is a function of the distance from the wall given by:

$$T^+ = \begin{cases} Pr\ y^+, & for\ y^+ \leq 11.81 \\ \dfrac{Pr_t}{\kappa}\ lny^+ + B_T, & for\ y^+ \geq 11.81 \end{cases} \quad (Equation\ 60)$$

where Pr and Pr_t are the molecular and turbulent Prandtl numbers and κ is the von Karman constant = 0.41. $T\tau$ is the temperature scale defined as:

$$T\tau \equiv \frac{\dot{q}_c''}{\rho c_p u_\tau} \quad (Equation\ 61)$$

B_T represents the resistance to heat and momentum transfer close to the wall and is a function of the Prandtl number as shown below:

$$B_T = \left(3.85Pr^{\frac{1}{3}} - 1.3\right)^2 + 2.12lnPr \quad (Equation\ 62)$$

Finally, the convective heat transfer coefficient can be obtained from the definition of h and T^+ above such that:

$$h = \frac{\dot{q}_c''}{T_g - T_w} = \frac{\rho c_p u_\tau}{T^+} \quad (Equation\ 63)$$

6   RESULTS & DISCUSSION

In this section the results of the numerical simulations will be analysed and compared to the experimental data for both the calcium silicate and plywood cases.

6.1   Heat Release Rate - Calcium silicate

Figure 12 below shows a comparison of the total HRR obtained in the simulations against the experimental data for calcium silicate (CSCS) experiment. The heat produced by the burner was specified in the FDS file by applying a burner surface at the top of the triangle and specifying a Heat Release Rate Per Unit Area (HRRPUA) of 960 kW/m^2.
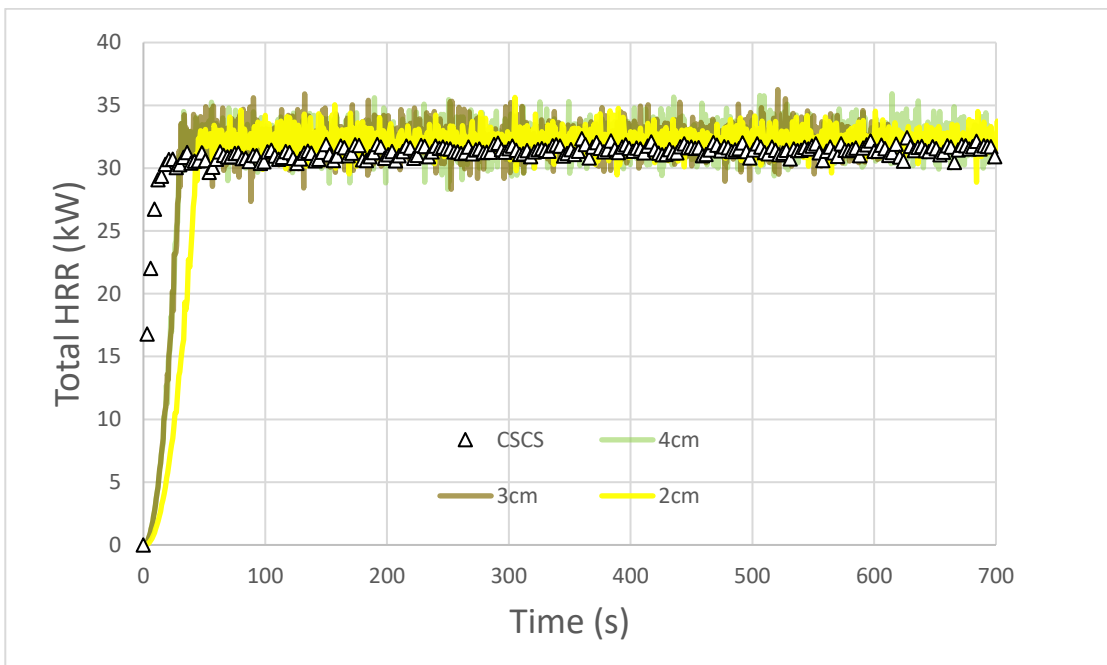

Figure 12 Total HRR from simulations versus those in the CSCS test.

Despite the triangle burner being composed of a series of rectangles it can be seen that for each of the cell sizes the HRR is predicted to reasonable degree of accuracy. The total HRR averages from 30- 700s for are slightly overestimate with values of 32 kW being calculated. It is likely that this slight overestimation is due to the snapping function of FDS where obstructions snap to the rectilinear grid, slightly increasing the dimensions of the burner and thus the HRR. It should also be noted that in the experimental data the HRR actual reaches the 30 kW in 20s as opposed to the quoted 30s accounting for the delay observed in the numerical studies. As the pyrolysis process does not occur in the inert CSCS test, the choice of convective heat transfer model has no influence on the total HRR.

6.1.1   Flame Heights

In the calcium silicate test the HRR from the burner goes to a steady state value after 30 seconds with a corresponding average flame height of 0.87m for the remainder of the test. Due to this steady state nature observed in the experiment for the HRR and flame heights, it

was attempted to model the flame heights in the simulation by placing 70 heat release rate per unit length (HRRPUL) devices in the vertical Z-axis. This provides a function of HRR/m vs height above the floor. This value was then integrated where the flame height is defined as the height at which the integrated HRR is 95% of the total HRR. The results for the flame height for each of the simulations are displayed below in Table 3.

Table 3 Flame heights from integration

Scenario	Flame Height (m)
Experiment	0.87
4cm Simulation	1.04(19.54%)
3cm Simulation	1.28(47.13%)
2cm Simulation	1.21(39.08)

As can be seen from Table 3, using the integrated HRR method the flame heights are overestimated for all the cell sizes. This error could be due to how the flame height is defined in the simulation as other parameters can be used to indicate the flame height such as gas temperatures or mixture fraction. It is also difficult to directly compare the flame heights between the experiments and the simulations as the experimental flame height is also dependent on the method used to quantify it.

Due to the difficulties outlined above, the instantaneous flame in each of the simulations and experimental work will be compared to qualitatively determine the accuracy of the numerical simulation to predict the flame heights.

Figure 13 shows that when comparing the experimental footage, the instantaneous flame heights from the simulations still overestimate the flame heights. The instantaneous flame heights fluctuate in the 3cm and 4cm simulation between 1.0m and 1.2m with occasional puffing extending the flame height to heights <1.4m. The 4cm in contrast ranges between 0.8m and 1.0m with the occasional fluctuation to heights <1.4m.

The experimental footage shows that the flame height for the most times remains between the 0.8m-1.0m with infrequent extensions increasing the height to circa 1.2m. Potential reasons for this discrepancy is due to the relatively complex shape of the burner in comparison to the more commonly studied circular and rectangular burners. It should be noted that in the FDS validation guide only a single triangular burner is assessed. Further experimental error could also be introduced due to parallax caused by the camera angle.

It is worth noting that when considering the R^* criteria, as outlined in section 3.2, only the 2cm simulation has an R^* of less than 0.1 for a 30kW fire. Whilst this criterion is used as a tool determine the cell size for free plumes it provides an indicative measure of *at least* the minimum cell size for a simulation in which the near wall effects will be modelled. Counterintuitively, the 4cm provides the most accurate flame heights although inaccuracies are when considering the heat flux of the fire as outlined below.
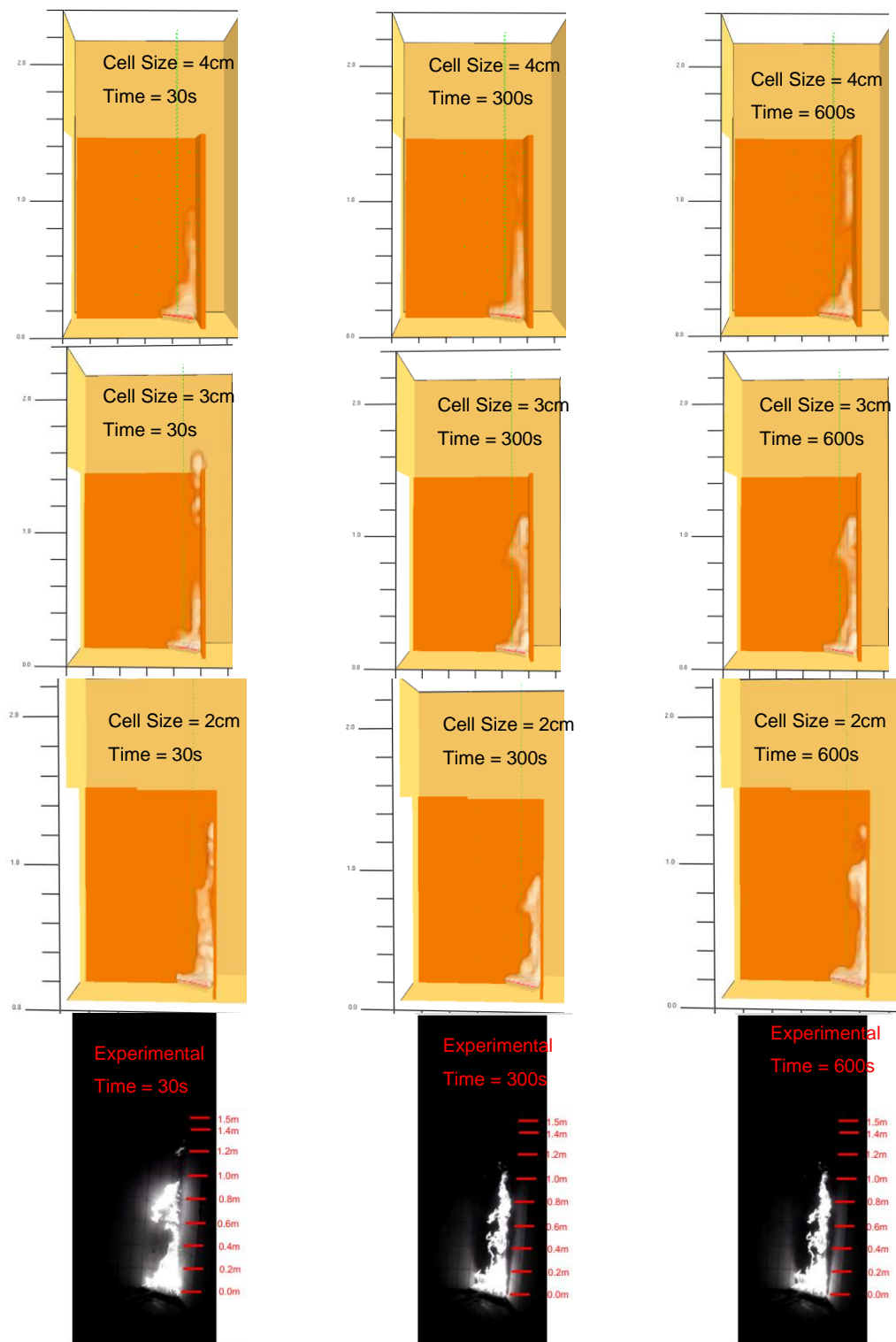
Figure 13 Comparison of instantaneous flame height for Calcium Silicate simulations and experiments. The heat release rate per unit volume (kW/m³) is considered for the visualisation of the flames.

6.1.2　Heat Flux measurements

The sensors are located at the same locations relative to the long panel as shown in figure 9 for the numerical simulations. The total heat fluxes were measured in the simulations using the Gauge Heat Flux option to attempt to simulate the response of the Schmidt-Boelter sensor in the experiments. The total heat flux calculated by the gauge is:

$$\dot{q}''_{gauge} = \varepsilon_{gauge}\left(\dot{q}''_{inc,rad} - \sigma T^4_{gauge}\right) + h(T_{gas} - T_{Gauge}) \quad (Equation\ 64)$$

where ε_{gauge} was taken as 0.9 and T_{Gauge} is 50°C as per the experiments [13]. As the HRR and flame heights become steady after approximately 30s until the end of the CSCS test the gauge heat fluxes will be averaged from 30s to 330s. Table 4 below displays the total gauge heat flux, incident heat flux and the convective heat flux for each of the cell sizes and convective heat transfer models. It should be noted that the values of the convective heat flux are calculated relative to the temperature of the surface as opposed to the gauge temperature as in Equation 64. However, it will provide an indicative measure of the total contribution by each of the heat transfer methods

Table 4. Gauge Heat Flux, Incident Heat Flux and Convective Heat Flux Measurements

Gauge Flux	Sensor 1 (kW/m^2)	Sensor 2 (kW/m^2)	Sensor 3 (kW/m^2)
Experimental	48.02	17.01	22.62
2cm Empirical	38.10(-20.65%)	5.86(-65.55%)	18.50(-18.21%)
2cm WM	39.19(-18.39%)	5.95(-65.02%)	21.69(-4.1%)
3cm Empirical	29.98(-37.67%)	6.22(-63.43%)	26.82(18.56%)
3cm WM	30.69 (-36.10%)	6.30(-62.96%)	30.53 (34.97%)
4cm Empirical	35.96(-25.11%)	7.09(-58.31%)	20.30(-10.26%)
4cm WM	35.60(-25.86%)	7.26(-57.31%)	22.42 (-0.88%)
Incident Heat Flux	Sensor 1 (kW/m^2)	Sensor 2 (kW/m^2)	Sensor 3 (kW/m^2)
2cm Empirical	33.01	6.23	14.83
2cm WM	33.66	6.29	15.01
3cm Empirical	26.78	6.52	21.28
3cm WM	26.89	6.56	21.63
4cm Empirical	32.13	7.44	15.46
4cm WM	32.03	7.61	15.21
Convective Heat Flux	Sensor 1 (kW/m^2)	Sensor 2 (kW/m^2)	Sensor 3 (kW/m^2)
2cm Empirical	3.87	0.03	2.36
2cm WM	3.94	-0.10	3.44
3cm Empirical	2.63	0.04	3.74
3cm WM	2.72	0.02	5.15
4cm Empirical	3.20	0.02	3.37
4cm WM	2.87	-0.02	4.10

*Values in brackets represent the percentage error when compared to experimental results.

When comparing the simulations to the experimental values the simulations tend to consistently underestimate the gauge heat fluxes. The heat fluxes at sensor 1 are most accurately predicted in the 2cm simulations although the percentage errors still range between 18-20%. The gauge heat flux at sensor 2 is significantly under predicted in all cases which is in line with the previous numerical studies into the SBI case [23,24] with percentage errors ranging between 57-65%. This is largely due to sensor 2 only intermittently being exposed to the flame. At sensor 3 the heat flux is reasonably predicted in both the 2cm and 4cm cases however in the 3cm cases the gauge heat flux is over predicted. The 3cm cases are the most inaccurate which could be due to the snapping function in FDS which snaps the burner closer to the wall with the distance being 0.03m between the wall and burner.

There are not significant differences between the choice of convective heat flux model on the total heat fluxes as shown in Table 4.The near wall model produces slightly higher heat fluxes in all the simulations and provides more slightly more accurate results for the 2cm and 4cm cases. It can be seen that the incident radiative heat flux is the most significant influence on the total gauge heat flux contributing in excess of 80% of the total gauge heat flux at sensors 1 and 3. At sensor 2 there is a negligible influence from the convective heat flux consistent with the flame/plume only being intermittently in this area for the numerical simulations and as thus only minor motion of fluid flow over this area.

6.2 Plywood Cases

6.2.1 Total Heat Release Rate

The plywood cases were initially simulated using the model effective thermal physical properties, as outlined in table 2, on a coarse 4cm grid as shown in figure 14 below.
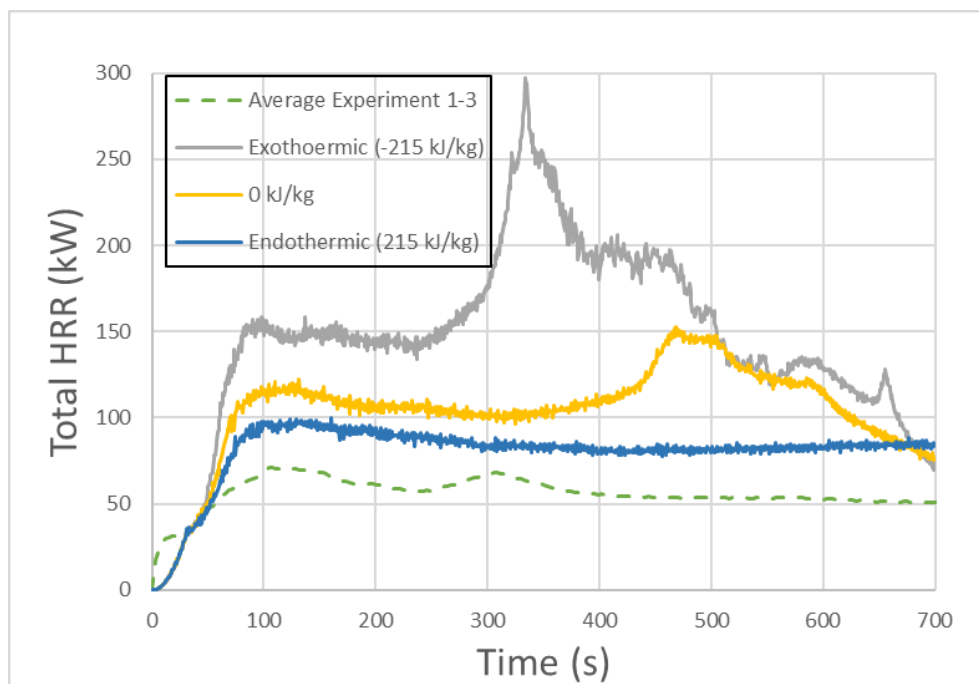

Figure 14 Total HRR – Influence of the heat of reaction

It can be seen that the default exothermic heat of reaction value derived via inverse modelling produces significantly higher HRR than what was recorded during the experimental tests. The peak HRR in this scenario is 300 kW which occurs at approximately 335s into the simulation. It is clear that this heat of reaction value is not suitable to attempt to model the surface flame spread on plywood using FDS v6.7.0. As no significant burning of the plywood was observed in the experiments, it can be deduced that the reaction may in fact be endothermic, these reactions are associated with the initial decomposition fuel and production of vapours. With endothermic reactions generally being associated in the later stages of char oxidation.

A sensitivity analysis was undertaken to determine how significantly the value of the heat of reaction will influence the total HRR in the simulation. Two cases were considered a heat of reaction value of 0 kJ/kg and an endothermic value of 215 kJ/kg which are shown above in

figure 14. It is clearly observed that the total HRR for both cases is significantly less than that of exothermic case, however both cases are still in excess of the averaged experimental value.

At 100 s which corresponds to the first peak in the experiments the 0 kJ/kg heat of reaction has a total HRR in excess of 40-50 kW whilst the endothermic value is 20-25 kW in excess of the experimental values. The two curves initially follow a similar trend with the HRR beginning to slowly decrease after about 200 seconds. However, in the 0 kJ/kg scenario begins to suddenly rise at 330 s until a peak HRR of 152 kW at 469s. The endothermic case tends toward a steady state condition with a near constant HRR of 80 kW. Whilst the endothermic case still produces significantly higher HRR in comparison to the experiments it follows a very similar trend. It can be inferred from this that for the modelling of the plywood pyrolysis process in FDS that an endothermic reaction is required.

Despite the simulation with the endothermic reaction having the general trend that follows the shape of the experimental HRR it still has significantly total higher heat output. In general, during the combustion of a wood sample there is little to no char oxidation in the first few minutes of the flaming fire, this is shown in cone calorimeter tests were the influence of the char only significantly contributes after 10 minutes [8]. As such it has been attempted to model the effective heat of combustion by assuming only the heat of combustion of pyrolysate. The value of 10.17 MJ/kg which was determined in an FPA test during the initial flaming period will be used herewith in the simulations. This value is very close to the derived value of 10.35 MJ/kg when assuming a value of 32.8 MJ/kg for the heat of oxidation of char in equation 53 which demonstrates the suitability of previous assumption that plywood has combustion efficiency of approximately 0.7. Using the heat of combustion of the pyrolysate is deemed a reasonable assumption as it was observed in the experimental data that after the reaction a dense char forms which acts as a thermal barrier causing the flame over the plywood to be non-self-sustaining meaning that it is the combustion pyrolysate is the dominant part of the HRR. Taking this into consideration the total HRR for the different convective heat transfer models is shown in figures 15.

Considering just the pyrolysate, the simulations still overestimate the total HRR for each of the cell sizes. The empirical model produces slightly lower HRR in comparison to the wall model due to the minor increases in convective heat fluxes calculated by the wall model(see section 6.1.2 and 6.2.3). In both cases, the larger the cell size the lower the total HRR although the difference is only around 5 kW. In all scenarios the HRR rapidly increases after the specified 30 kW from the burner is reached as is also observed in the experimental data. All the scenarios replicate the experimental result for the initial 100s after which the simulations exceed the HRR of the experiments. The simulations whilst produce a peak at around the same time as the experiments they do not however, provide a second peak due to the lateral flame spread. in contrast the simulations remain at the peak value for another 30 seconds prior to slowly decreasing.
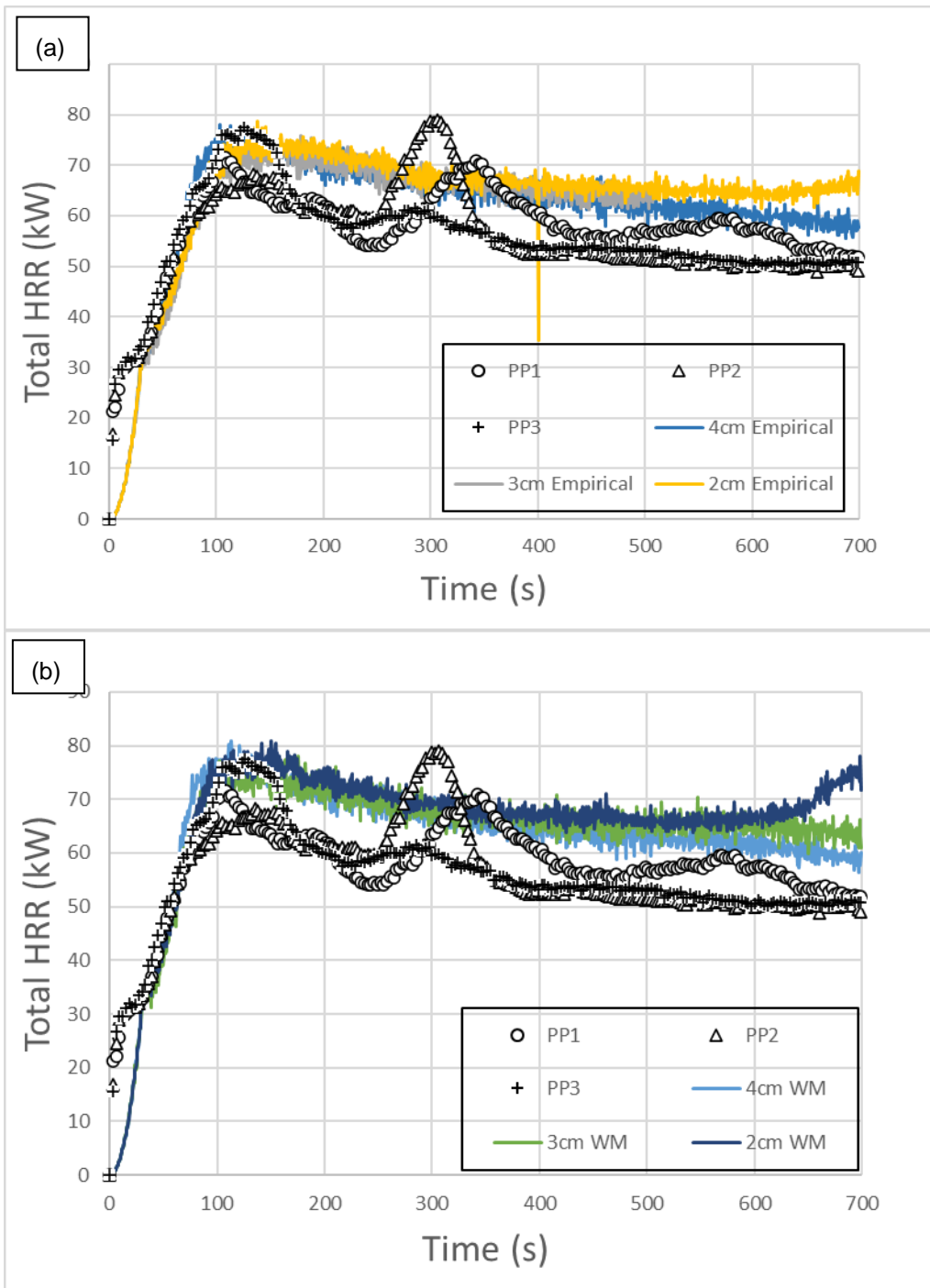
Figure 15 . Comparison between the predicted HRR and Experimental HRR. Figure (a) shows the results for the empirical model with (b) showing the results for the wall model.

6.2.2 Backside flaming

A significant influence in the HRR is that in each of the simulations back side flaming was observed as shown below in figure 16. Minor backside flaming begins to occur at around the 420s in the 2cm with a slight delay in the 3cm and 4cm cases, this is shown when both convective heat transfer models are applied.
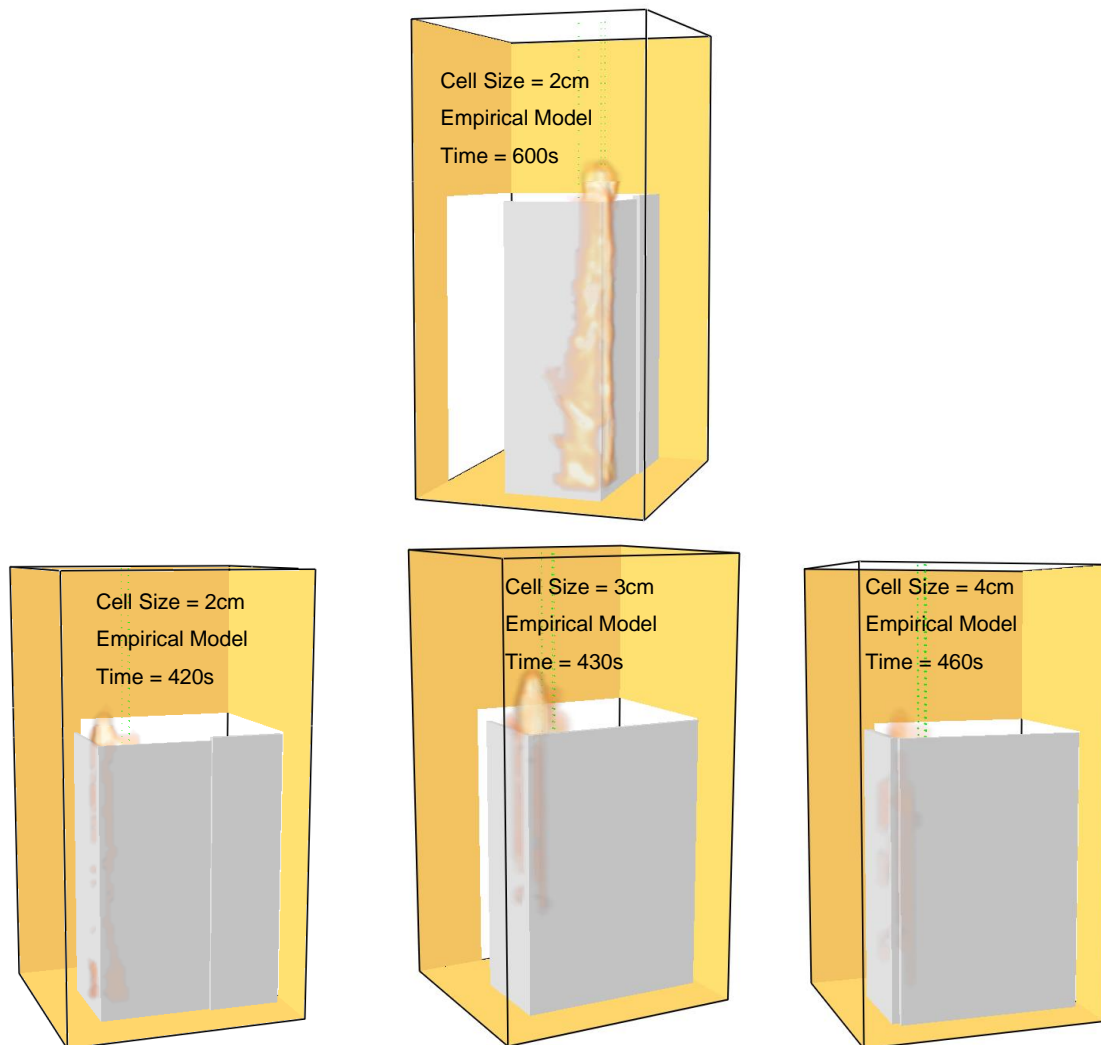
Figure 16 Evidence of backside flaming in numerical simulations. The heat release rate per unit volume (kW/m³) is considered for the visualisation of the flames.

Significant flames develop on the backside in the 2cm cases at approximately 600s which is reflected by the increase in HRR at this time as shown in figure 15. This contrasts with the experiments where the corner was compromised only in experiments 1 & 3 at times in excess of 1000s. The numerical results can be interpreted through the thermal penetration time of the plywood where:

$$t_p = \frac{L^2}{4\alpha} \; ; \; \alpha = \frac{k}{\rho c} \; (Equation\ 65)$$

where L is the thickness (m), α is the thermal diffusivity (m²/s), k is the thermal conductivity (w/mK), ρ is the density of the material (kg/m³), c is the specific heat (J/kg·K).

The thermal penetration time represents the time at which 15% of the temperature increase on the fire-exposed side has reached the non-exposed side [7]. Considering equation 65 for the plywood, a thermal penetration time of 448s is calculated however this is overtly conservative as it assumes non transient conditions and that the plywood is inert. The char as described by the model effective parameters has a significantly higher thermal diffusivity and thus a lower penetration time than the virgin plywood. It can be inferred from this that once the reaction occurs and char is produced the thermal penetration time will decrease as reflected in the numerical simulations. It should also be noted that in the experiments a dense char was

formed during the course of the tests, this is also shown by the averaged cone calorimeter data of the plywood samples showing that the bulk density of the plywood char is around 223 kg/m^3 [12]. This is significantly higher than the model effective parameter of 82 kg/m^3. The increased density of char will also affect the thermal inertia of the solid were an increased thermal inertia results in a higher resistance to temperature change. When considering equation 65 the higher density will decrease the diffusivity and subsequently increase the thermal penetration time.

6.2.3   Heat flux measurements

Figure 17 shows the total heat fluxes in each of the simulations and compares them to the experimental data. The general trend of the plywood simulations is similar to the inert cases. At sensor 1 the measured heat flux tends to be higher for smaller the cell sizes, however the total heat flux at this point is still underestimated when compared to the experimental data. Similarly to the CSCS tests, the heat fluxes are significantly under predicted at sensor 2. From 300s onwards the heat fluxes are under predicted by approximately 10 – 20 kW/m^2 with the large increase in heat flux at the beginning stages due to lateral flame [12] spread not being accounted for. The heat flux at sensor 3 is reasonably well predicted for each of the convective heat transfer models.

In each of the scenarios, the wall model produces total higher heat fluxes when compared with the empirical model. However, these higher heat fluxes will result in an increase of the rate of pyrolysis resulting in a higher total HRR as shown in section 6.2.1.

It is a non-intuitive result that the lower heat fluxes in the numerical works result in higher total HRR when compared to the experimental results. This can be caused by a variety of reasons as identified above in section 6.2.2. It should also be noted that the flame heights (see section 6.2.4) are consistently higher than the experimental results and this could potentially increase the pyrolysis in the upper section of the board and also cause backside pyrolysis in this location contributing to the overall predicted HRR.

This excessive increase in back side temperature and HRR can also be understood via equation 46 and 53.

$$\rho_s c_s \frac{\partial T_s}{\partial t} = \frac{\partial}{\partial x}\left(k_s \frac{\partial T_s}{\partial x}\right) + (\dot{q}_{s,c}''' + \dot{q}_{s,r}''')\ (Equation\ 46)$$

The total energy stored by the material $\rho_s c_s \frac{\partial T_s}{\partial t}$ due to a bulk temperature change over the time is directly related to the source term $\dot{q}_{s,c}'''$:

$$\dot{q}_{s,c}''' = -\rho_v \left(A_{ab} Y_{s,a}^{n_{s,ab}} \exp\left(-\frac{E_{ab}}{RT_s}\right)\right) H_p\ (Equation\ 53)$$

Considering this, it can be deduced that the endothermic heat of reaction H_p values used in the simulations are not high enough to avoid the excessive temperature rise in the plywood case which will have a direct influence on the HRR. With this value being the largest influence on the predicted results. This value should be extensively studied in future studies.
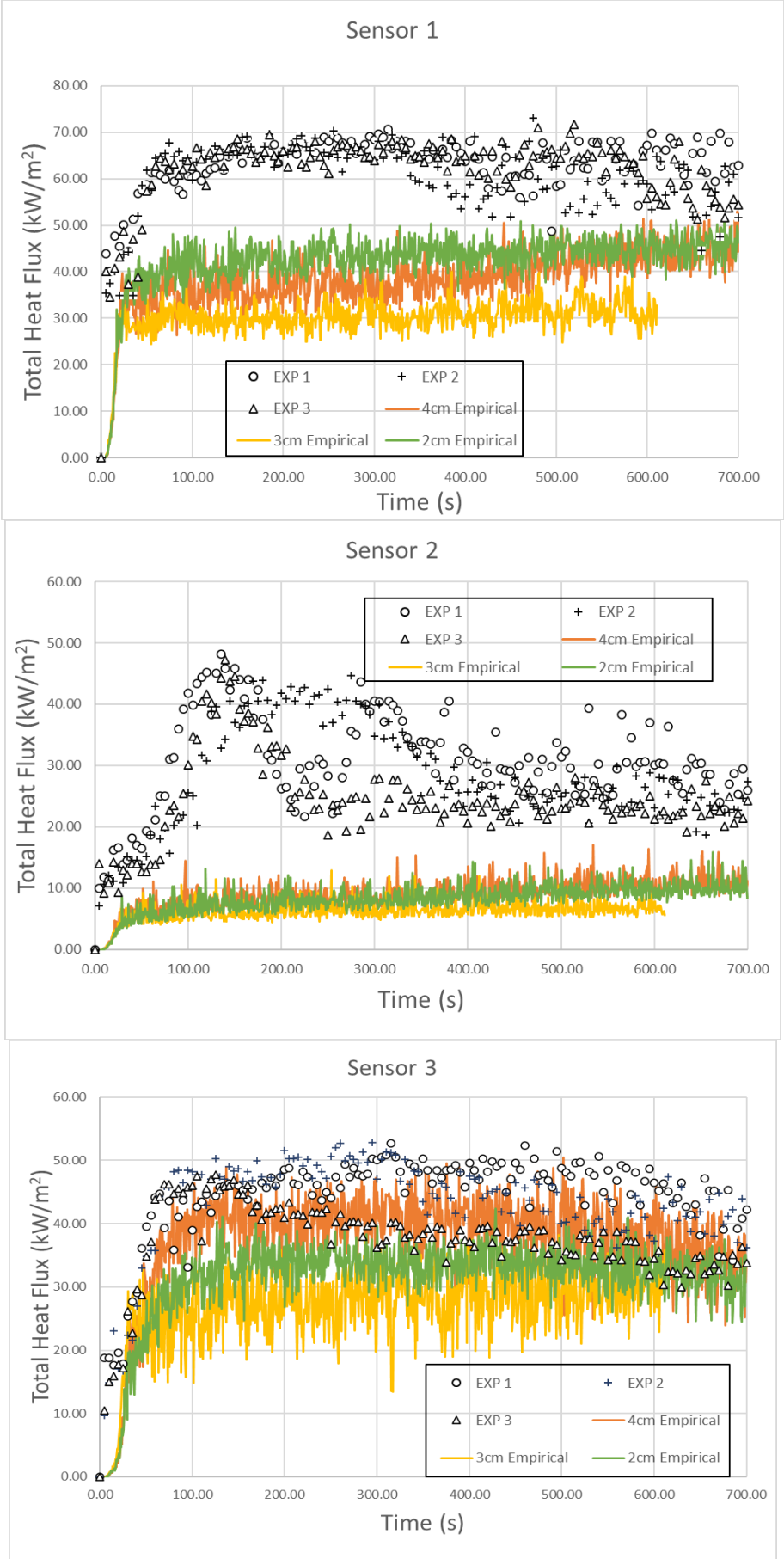
Figure 17 Comparison between experimental and numerical simulations for the measured heat fluxes using the empirical convective heat transfer model.
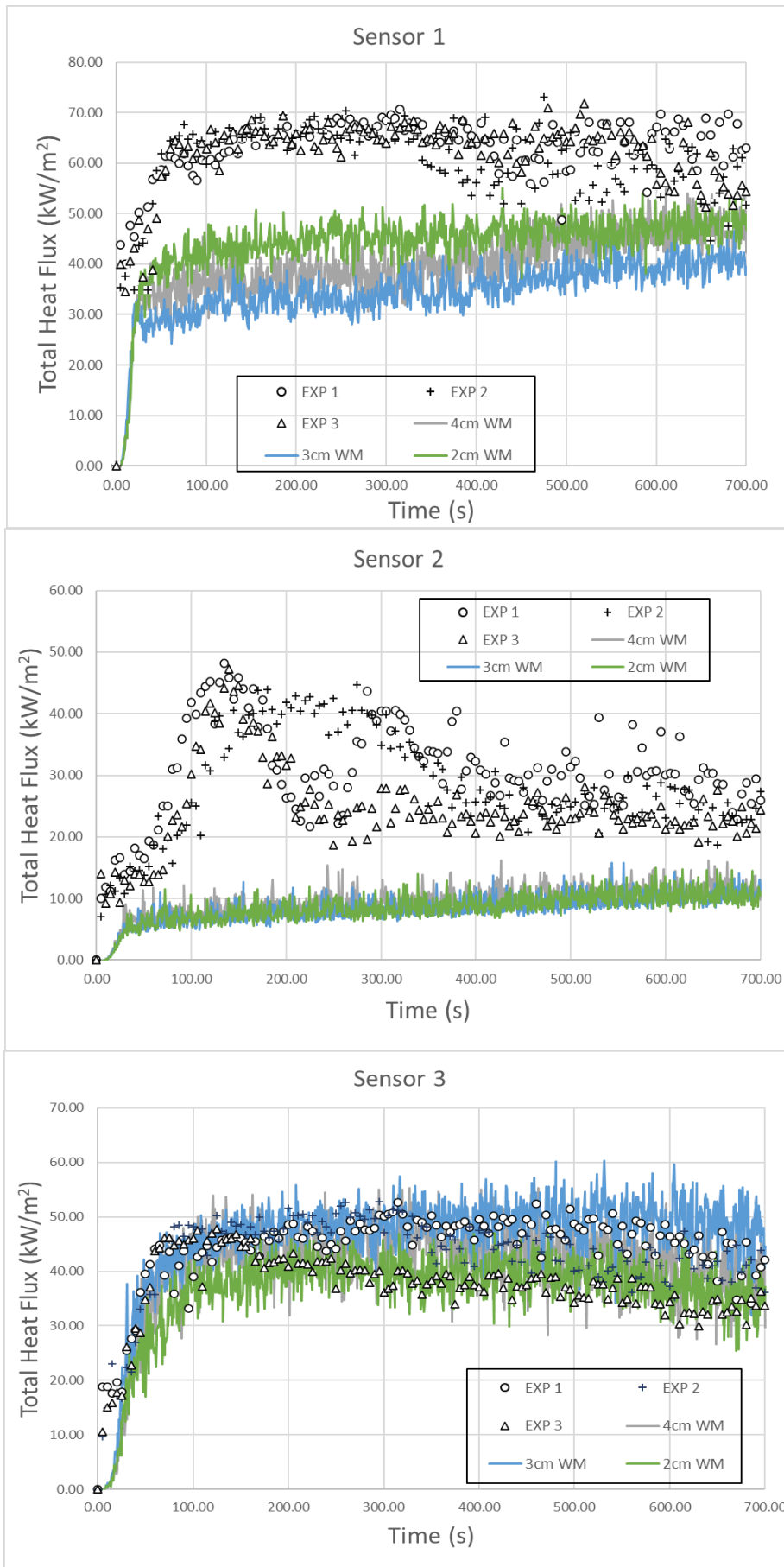
Figure 18 Comparison between experimental and numerical simulations for the measured heat fluxes using wall model.

6.2.4   Flame Heights, Flame Spread and Pyrolysis front

Figure 18 below shows a series of snap shots of the flame heights and lateral flame spread of the 2cm simulations and experimental data of Experiment 1. It should be noted that the other cell sizes reproduce similar results although the 4cm results show slightly lower results.
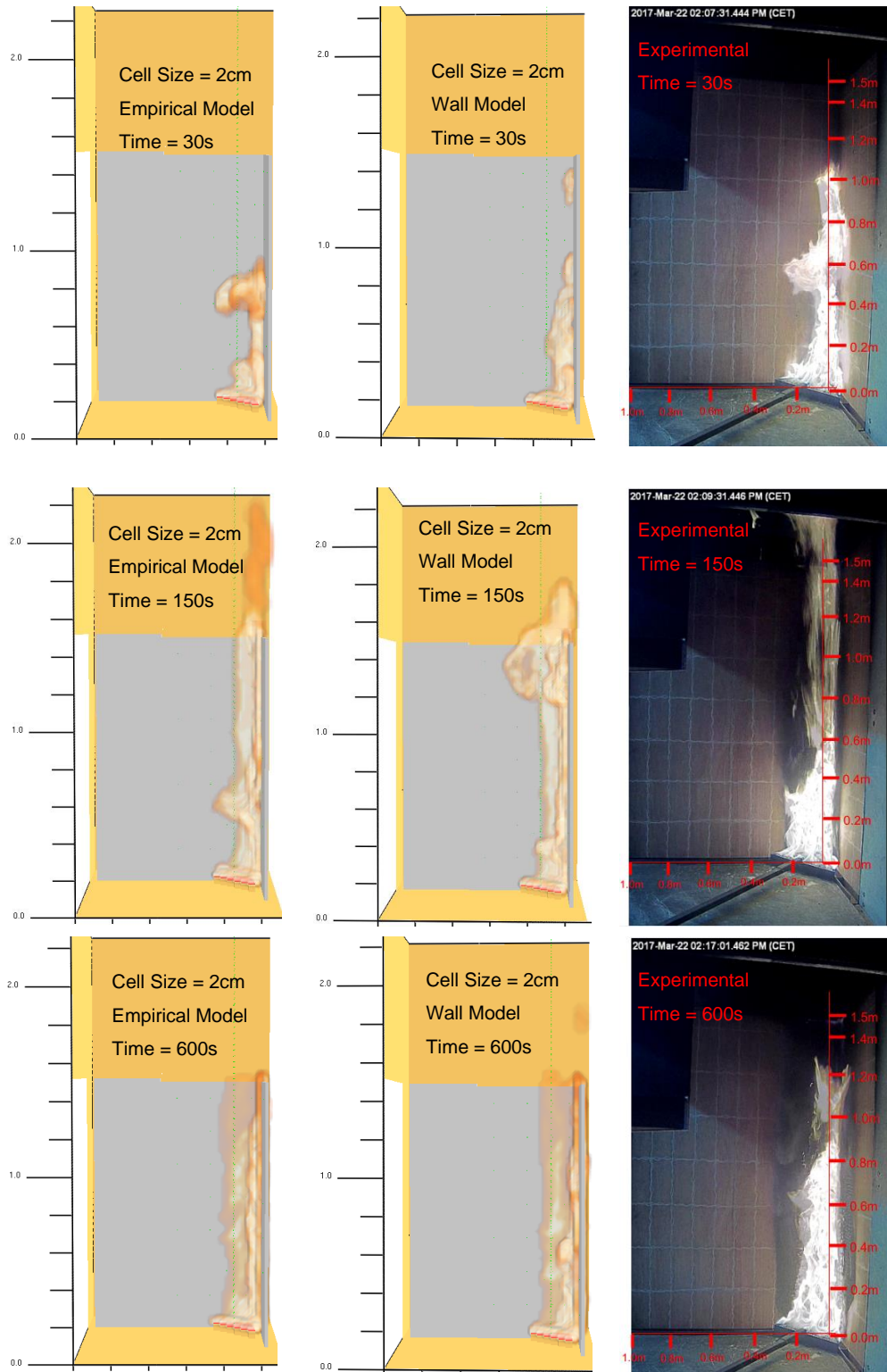

Figure 19 Comparison of the long panel view of flame spread between plywood simulations and experimental. The heat release rate per unit volume (kW/m³) is considered for the visualisation of the flames.

In both convective heat transfer methods, the flame heights from 100-300s fluctuate from 1.6 to 2.2m. At this time period in experimental tests, the flame heights exceed the 1.5m of the panel although it is not possible to accurately assess the experimental values during this time as the footage height is limited to approximately 1.6m. After this time period the flame height of the simulations drops to between 1.6m and 1.8 m. Compared to the experiments, at this time period the simulations have an averaged flame height of 1.2m although there are still fluctuations evident which exceed the 1.6m. The overpredicted flame heights are likely due to the points raised in sections 6.2.1 – 6.2.3. It should also be recognised that as illustrated in the calcium silicate tests, FDS appears to overestimate the flame height in corners even when pyrolysis is not considered.

The lateral flame spread in the simulations is rather similar to the experimental data with a general u/v shape forming. The burner is clearly the biggest influence on the flaming as the lateral flame spread does not extend beyond the dimensions of the burner, suggesting that as per the experimental results the plywood produces a flame that is not self-sustaining.

As discussed in section 2,2 the pyrolysis of wood products tends to occur at temperatures in the range of 200-300 $^{\circ}$C. In this analysis pyrolysis front will be determined by analysing the wall temperature of the boundary file produced in FDS. The pyrolysis front will be defined where surface temperature is 200 $^{\circ}$C as a conservative measure. It should be noted that this is a crude method in determining the pyrolysis as the onset pyrolysis is determined by the reaction kinetics. However, it will provide an indicative measurement.

The black lines in figure 20 indicate the location where a wall temperature of 200 $^{\circ}$C is obtained. When the wall model is used to calculate the convective heat transfer the pyrolysis is slightly more extensive as would be expected due to the higher heat fluxes as outlined in section 6.2.3. A general U pattern develops during the simulations for the pyrolysis zone. When compared to the experiments, the pyrolysis fronts are predicted relatively well as the pyrolysis front was noted to extend a maximum of 0.32m from the corner on the long panel for experiments 1 & Experiments 2. It should be noted that this occurs at roughly 400s into the experiments whilst it occurs at around 150 s in the simulations.
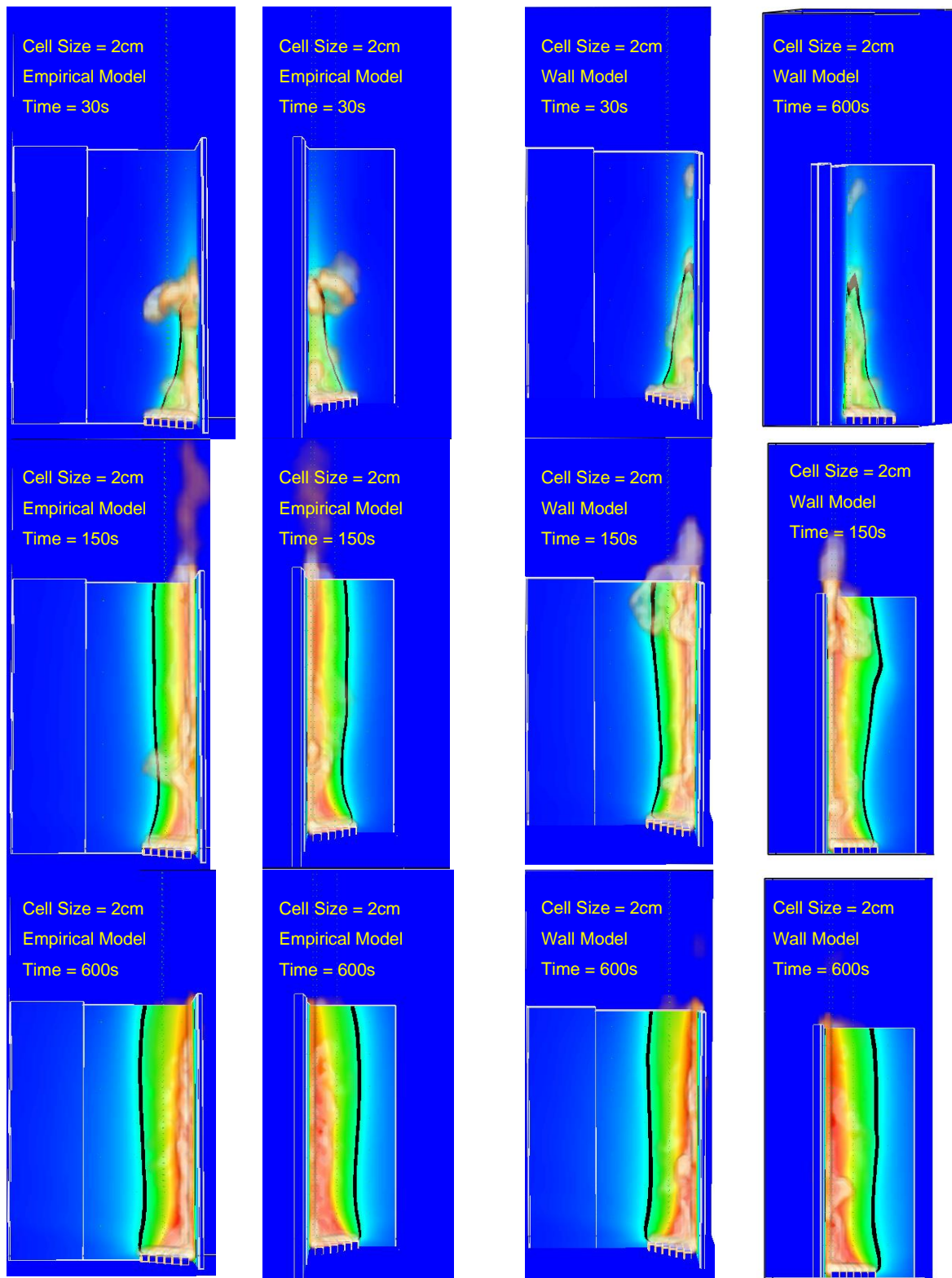
Figure 20 Pyrolysis fronts. (a) and (b) represents the of the long and short panels for the empirical correlation. With (c) and (d) represent the long and short panel for the wall model.

7 <u>CONCLUSION</u>

Numerical simulations were performed using FDS v6.7.0 to simulate the experimental work previously conducted at the University of Ghent. The simulations attempted to evaluate how well the CFD code could predict the thermal impact that a triangle burner would have on calcium silicate and plywood panels. An emphasis of this study was to investigate how the connective heat transfer models would influence the results.

The calcium silicate simulations showed that the flame heights consistently over predicted by FDS when compared to the experimental results. As the size of the cells was decreased the solution would become more accurate however the fluxes were still significantly underrated. There was only a minor difference noticed when changing the convective heat transfer model with the wall model providing slightly more accurate results.

It was attempted to simulate the pyrolysis process in the plywood panels by using model effective properties. These values were developed by the inverse modelling of bench scale tests. These simulations significantly over predicted the HRR as such a sensitivity analysis was conducted demonstrating that the pyrolysis reaction of plywood should be modelled as an endothermic reaction as opposed to an exothermic one. A study was also conducted on the influence of the heat of combustion, due to the minor influence of char oxidation at the beginning of the experiment as such the heat of combustion of the pyrolyzate was used in the remaining experiments. In these simulations the predicted total HRR still noticeably exceeded that of the experimental values. The total heat fluxes were underpredicted on the board as per the calcium silicate tests with the wall model producing slightly higher results. Backside flaming was observed in the simulations at times corresponding to the thermal penetration time of virgin plywood. This concept was used to explain why back side flaming occurred with the density of the model effective char being identified as a potential factor. The total flame heights of the plywood scenario exceeded the experimental results in all cases likely due to aforementioned errors associated with the HRR. The lateral flame spread and pyrolysis front compared comparatively well with experimental results. As the flame and pyrolysis fronts did not extend beyond the boundaries of the burner it can be deduced that for the modelled reaction the fire is not self-sustaining.

In the future a step wise approach should be adopted in FDS simulating bench scale tests in order to inversely model the effective properties for specific use in FDS. Upon the development of new model effective properties other areas of study that should be considered are the influence of more complex radiation models and the influence of temperature dependent properties such as the emissivity of the materials. The full effects of the char oxidation should also be considered despite the heat of combustion of the pyrolyzate being considered for the majority of the simulations, cracking in the char is noticed in the experimental footage 6 minutes into the test.

8 REFERENCES

[1]   Grenfell Tower: What happened - BBC News, (n.d.). https://www.bbc.com/news/uk-40301289 (accessed February 13, 2020).

[2]   Russia fire: Children killed in Kemerovo shopping centre blaze - BBC News, (n.d.). https://www.bbc.com/news/world-europe-43531684 (accessed February 13, 2020).

[3]   How it happened: Notre Dame Cathedral fire - CNN, (n.d.). https://edition.cnn.com/world/live-news/notre-dame-fire/index.html (accessed February 13, 2020).

[4]   The house made of wood - Why more buildings should be made of wood | Leaders | The Economist, (n.d.). https://www.economist.com/leaders/2019/01/05/why-more-buildings-should-be-made-of-wood (accessed February 13, 2020).

[5]   D. Thomas, G. Ding, K. Crews, Sustainable timber use in residential construction: Perception versus reality, WIT Trans. Ecol. Environ. 186 (2014) 399–410. https://doi.org/10.2495/ESUS140341.

[6]   wooden skyscrapers: a roundup of tall timber buildings, (n.d.). https://www.designboom.com/architecture/wooden-skyscrapers-timber-tower-construction-roundup-07-31-2016/ (accessed February 13, 2020).

[7]   B. Karlsson, J.G. Quintiere, Enclosure fire, 1999.

[8]   D. Drysdale, An Introduction to Fire Dynamics: Third Edition, 2011. https://doi.org/10.1002/9781119975465.

[9]   J. Hietaniemi, S. Hostikka, J. Vaari, FDS simulation of fire spread – comparison of model results with experimental data, VTT Build. Transp. (2004).

[10]   M. Poreh, G. Garrad, Study of wall and corner fire plumes, Fire Saf. J. (2000). https://doi.org/10.1016/S0379-7112(99)00040-5.

[11]   FDS and Smokeview | NIST, (n.d.). https://www.nist.gov/services-resources/software/fds-and-smokeview (accessed April 28, 2020).

[12]   D. Zeinali, Flame spread and fire behavior in a corner configuration, Ghent University. Faculty of Engineering and Architecture, 2019.

[13]   D. Zeinali, S. Verstockt, T. Beji, G. Maragkos, J. Degroote, B. Merci, Experimental study of corner fires — Part I: Inert panel tests, 0 (2017) 1–19. https://doi.org/10.1016/j.combustflame.2017.09.034.

[14]   D. Zeinali, S. Verstockt, T. Beji, G. Maragkos, J. Degroote, B. Merci, Experimental study of corner fires — Part II : Flame spread over MDF panels, Combust. Flame. 189 (2018) 491–505. https://doi.org/10.1016/j.combustflame.2017.10.023.

[15]   D. Zeinali, G. Agarwal, A. Gupta, G. Maragkos, T. Beji, M. Chaos, Y. Wang, N. Ren, J. Degroote, B. Merci, Computational Analysis of Pyrolysis and Flame Spread for MDF Panels Placed in a Corner Configuration, (n.d.) 385–394. https://doi.org/10.20285/c.sklfs.8thISFEH.039.

[16]   D. Zeinali, A. Gupta, G. Maragkos, G. Agarwal, T. Beji, M. Chaos, Y. Wang, J. Degroote, B. Merci, M.S. Division, L. Livermore, E. Avenue, P.O. Box, Study of the importance of non-uniform mass density in numerical simulations of fire spread over MDF panels in a corner configuration, Combust. Flame. 200 (2019) 303–315. https://doi.org/10.1016/j.combustflame.2018.11.020.

[17]   A. Trouvé, Y. Wang, Large eddy simulation of compartment fires, Int. J. Comut. Fluid Dyn. (2010). https://doi.org/10.1080/10618562.2010.541393.

[18]   N. Ren, Y. Wang, A. Trouvé, Large eddy simulation of vertical turbulent wall fires, in: Procedia Eng., 2013. https://doi.org/10.1016/j.proeng.2013.08.086.

[19]   N. Ren, Y. Wang, S. Vilfayeau, A. Trouvé, Large eddy simulation of turbulent vertical wall fires supplied with gaseous fuel through porous burners, Combust. Flame. (2016). https://doi.org/10.1016/j.combustflame.2015.12.008.

[20]   E. Markus, A. Snegirev, E. Kuznetsov, L. Tanklevskiy, Application of the thermal pyrolysis model to predict flame spread over continuous and discrete fire load, Fire Saf. J. (2019). https://doi.org/10.1016/j.firesaf.2019.102825.

[21]   E. Markus, A. Snegirev, E. Kuznetsov, L. Tanklevskiy, Application of a simplified

pyrolysis model to predict fire development in rack storage facilities, in: J. Phys. Conf. Ser., 2018. https://doi.org/10.1088/1742-6596/1107/4/042012.

[22] H.Y. Wang, M. Coutin, J.M. Most, Large-eddy-simulation of buoyancy-driven fire propagation behind a pyrolysis zone along a vertical wall, Fire Saf. J. (2002). https://doi.org/10.1016/S0379-7112(01)00050-9.

[23] G. Zhao, Numerical Study on Under-Ventilated Enclosure Fires and Fire Spread on Building Façades, 2017.

[24] J. Zhang, M. Delichatsios, M. Colobert, Assessment of fire dynamics simulator for heat flux and flame heights predictions from fires in SBI tests, Fire Technol. (2010). https://doi.org/10.1007/s10694-008-0072-6.

[25] M.J. Moran, H.N. Shapiro, Fundamentals of Engineering Thermodynamics, 5th Edition, 2006. https://doi.org/10.1038/1811028b0.

[26] A. Atreya, Convection heat transfer, in: SFPE Handb. Fire Prot. Eng. Fifth Ed., 2016. https://doi.org/10.1007/978-1-4939-2565-0_3.

[27] J. Torero, Flaming ignition of solid fuels, in: SFPE Handb. Fire Prot. Eng. Fifth Ed., 2016. https://doi.org/10.1007/978-1-4939-2565-0_21.

[28] A. Witkowski, A.A. Stec, T.R. Hull, Thermal decomposition of polymeric materials, in: SFPE Handb. Fire Prot. Eng. Fifth Ed., 2016. https://doi.org/10.1007/978-1-4939-2565-0_7.

[29] D. Drysdale, An Introduction to Fire Dynamics: Third Edition, 2011. https://doi.org/10.1002/9781119975465.

[30] J.G. Quintiere, Fundamentals of Fire Phenomena, 2006. https://doi.org/10.1002/0470091150.

[31] G. Heskestad, Fire plumes, flame height, and air entrainment, in: SFPE Handb. Fire Prot. Eng. Fifth Ed., 2016. https://doi.org/10.1007/978-1-4939-2565-0_13.

[32] Y. Hasemi, Surface flame spread, in: SFPE Handb. Fire Prot. Eng. Fifth Ed., 2016. https://doi.org/10.1007/978-1-4939-2565-0_23.

[33] D.D. Drysdale, Ignition of liquids, in: SFPE Handb. Fire Prot. Eng. Fifth Ed., 2016. https://doi.org/10.1007/978-1-4939-2565-0_18.

[34] B.Y. Lattimer, U. Sorathia, Thermal characteristics of fires in a noncombustible corner, Fire Saf. J. (2003). https://doi.org/10.1016/S0379-7112(03)00065-1.

[35] B.Y. Lattimer, U. Sorathia, Thermal characteristics of fires in a combustible corner, Fire Saf. J. (2003). https://doi.org/10.1016/S0379-7112(03)00066-3.

[36] W. Takahashi, O. Sugawa, H. Tanaka, M. Ohtake, Flame And Plume Behavior In And Near A Corner Of Walls, Fire Saf. Sci. (1997). https://doi.org/10.3801/iafss.fss.5-261.

[37] B. Merci, T. Beji, Fluid mechanics aspects of fire and smoke dynamics in enclosures, 2016. https://doi.org/10.1201/b21320.

[38] J.H. Ferziger, M. Peric, A. Leonard, Computational Methods for Fluid Dynamics, Phys. Today. (1997). https://doi.org/10.1063/1.881751.

[39] V. Novozhilov, Computational fluid dynamics modeling of compartment fires, Prog. Energy Combust. Sci. (2001). https://doi.org/10.1016/S0360-1285(01)00005-3.

[40] S. Miles, Modeling fires using computational fluid dynamics (cfd), in: SFPE Handb. Fire Prot. Eng. Fifth Ed., 2016. https://doi.org/10.1007/978-1-4939-2565-0_32.

[41] K.B. McGrattan, Fire dynamics simulator Technical Reference Guide Volume 1: Mathematical Model, 2019. https://doi.org/10.6028/NIST.SP.1018.

[42] R. McDermott, K. McGrattan, S. Hostikka, J. Floyd, Fire Dynamics Simulator (Version 5) Technical Reference Guide: Validation, 2010.

[43] K.B. McGrattan, S. Hostikka, J.E. Floyd, Fire dynamics simulator (version 6), user's guide, NIST Spec. Publ. (2014).

[44] K. McGrattan, S. Hostikka, R. McDermott, J. Floyd, M. Vanella, Fire Dynamics Simulator User's Guide, NIST Spec. Publ. 1019 Sixth Ed. (2019). https://doi.org/10.6028.

[45] X. Huang, K. Li, H. Zhang, Modelling bench-scale fire on engineered wood: Effects of transient flame and physicochemical properties, Proc. Combust. Inst. (2017). https://doi.org/10.1016/j.proci.2016.06.109.

[46] H.C. Kung, A.S. Kalelkar, On the heat of reaction in wood pyrolysis, Combust. Flame.

(1973). https://doi.org/10.1016/S0010-2180(73)81260-X.

[47]   V. Babrauskas, Effective heat of combustion for flaming combustion of conifers, Can. J. For. Res. (2006). https://doi.org/10.1139/x05-253.

[48]   A. Tewarson, Generation of Heat and Chemical Compounds in Fires, in: SFPE Handb. Fire Prot. Eng. - Third Ed., 2002.

9 APPENDIX

9.1   Sample FDS File

&HEAD CHID='Simplified_Geometry_Plywood_2cm'/
&TIME T_END=700/
&DUMP DT_RESTART=100.0, DT_SL3D=0.25/

&MESH ID='MESH1', IJK=42,44,80, XB=-0.32,0.52,0.52,1.4,0.0,1.6, MPI_PROCESS=0,
N_THREADS=3/
&MESH ID='MESH2', IJK=21,22,20, XB=-0.32,0.52,0.52,1.4,1.6,2.4, MPI_PROCESS=1/
&MESH ID='MESH3', IJK=21,22,60, XB=-0.32,0.52,0.08,0.52,0.0,2.4, MPI_PROCESS=2/
&MESH ID='MESH4', IJK=9,33,60, XB=0.52,0.88,0.08,1.4,0.0,2.4, MPI_PROCESS=3/

&REAC ID='Propane',
    FUEL='PROPANE',
    RADIATIVE_FRACTION=0.3/

&MATL ID='CHAR',
    EMISSIVITY=0.85,
    SPECIFIC_HEAT=1.45,
    CONDUCTIVITY=0.19,
    DENSITY=82.0,/

&MATL ID='Plywood',
    EMISSIVITY=0.9,
    SPECIFIC_HEAT=1.32956,
    CONDUCTIVITY=0.12,
    DENSITY=560.0,
    N_REACTIONS=1,
    A=6.3E4,
    E=8.02E4,
    MATL_ID ='CHAR',
    NU_MATL = 0.15,
    SPEC_ID='PROPANE',
    NU_SPEC =0.85,
    HEAT_OF_REACTION=215.0,
        HEAT_OF_COMBUSTION=10170/

&SURF ID='Ply',
    COLOR='GRAY 80',
    MATL_ID ='Plywood',
    MATL_MASS_FRACTION =1.0,
    THICKNESS =0.017,
    STRETCH_FACTOR=1/

&SURF ID='Burner',
    COLOR='RED',
    HRRPUA=960.0,

TAU_Q=-30.0/

&OBST ID='1.0m Panel', XB=-0.0132,0.0,0.12,1.1332,0.0,1.5, THICKEN=.TRUE., SURF_ID='Ply'/
&OBST ID='0.5m Panel', XB=0,0.5,1.12,1.1332,0.0,1.5, THICKEN=.TRUE., SURF_ID='Ply'/
&OBST ID='Burner', XB=0.04,0.08,0.84,0.88,0.0,0.04, SURF_IDS='Burner','INERT','INERT'/
&OBST ID='Burner', XB=0.04,0.12,0.88,0.92,0.0,0.04, SURF_IDS='Burner','INERT','INERT'/
&OBST ID='Burner', XB=0.04,0.16,0.92,0.96,0.0,0.04, SURF_IDS='Burner','INERT','INERT'/
&OBST ID='Burner', XB=0.04,0.2,0.96,1.0,0.0,0.04, SURF_IDS='Burner','INERT','INERT'/
&OBST ID='Burner', XB=0.04,0.24,1.0,1.04,0.0,0.04, SURF_IDS='Burner','INERT','INERT'/
&OBST ID='Burner', XB=0.04,0.28,1.04,1.08,0.0,0.04, SURF_IDS='Burner','INERT','INERT'/

&VENT ID='Mesh Vent: MESH [ZMAX]', SURF_ID='OPEN', XB=-0.32,0.88,0.08,1.4,2.4,2.4/
&VENT ID='Mesh Vent: MESH [XMAX]', SURF_ID='OPEN', XB=0.88,0.88,0.08,1.0,0.0,1.5/
&VENT ID='Mesh Vent: MESH [YMIN]', SURF_ID='OPEN', XB=0.04,0.88,0.08,0.08,0.0,1.5/

&PROP ID='hfp', GAUGE_TEMPERATURE=50., GAUGE_EMISSIVITY=0.9 /

&DEVC ID='Sensor 1 Qrad X', QUANTITY='RADIATIVE HEAT FLUX', XYZ=0.0,1.04,0.2, IOR=1/
&DEVC ID='Sensor 1 Qconv', QUANTITY='CONVECTIVE HEAT FLUX', XYZ=0.0,1.04,0.2, IOR=1/
&DEVC ID='Sensor 1 Incident Heat Flux', QUANTITY='INCIDENT HEAT FLUX', XYZ=0.0,1.04,0.2, IOR=1/
&DEVC ID='Sensor 1 Heat Flux', QUANTITY='NET HEAT FLUX', XYZ=0.0,1.04,0.2, IOR=1/
&DEVC ID='Sensor 1 total', XYZ=0.0,1.04,0.2, IOR=1,QUANTITY='GAUGE HEAT FLUX', PROP_ID='hfp' /

&DEVC ID='Sensor 3 Qrad', QUANTITY='RADIATIVE HEAT FLUX', XYZ=0.0,1.04,0.8, IOR=1/
&DEVC ID='Sensor 3 Qconv', QUANTITY='CONVECTIVE HEAT FLUX', XYZ=0.0,1.04,0.8, IOR=1/
&DEVC ID='Sensor 3 Incident Heat Flux', QUANTITY='INCIDENT HEAT FLUX', XYZ=0.0,1.04,0.8, IOR=1/
&DEVC ID='Sensor 3 Heat Flux', QUANTITY='NET HEAT FLUX', XYZ=0.0,1.04,0.8, IOR=1/
&DEVC ID='Sensor 3 total', XYZ=0.0,1.04,0.8, IOR=1,QUANTITY='GAUGE HEAT FLUX', PROP_ID='hfp' /

&DEVC ID='Sensor 2 Qrad', QUANTITY='RADIATIVE HEAT FLUX', XYZ=0.0,0.92,0.35, IOR=1/
&DEVC ID='Sensor 2 Qconv', QUANTITY='CONVECTIVE HEAT FLUX', XYZ=0.0,0.92,0.35, IOR=1/
&DEVC ID='Sensor 2 Incident Heat Flux', QUANTITY='INCIDENT HEAT FLUX', XYZ=0.0,0.92,0.35, IOR=1/
&DEVC ID='Sensor 2 Heat Flux', QUANTITY='NET HEAT FLUX', XYZ=0.0,0.92,0.35, IOR=1/
&DEVC ID='Sensor 2 Total', XYZ=0.0,0.92,0.35, IOR=1,QUANTITY='GAUGE HEAT FLUX', PROP_ID='hfp' /

&BNDF QUANTITY='WALL TEMPERATURE'/
&BNDF QUANTITY='INCIDENT HEAT FLUX'/
&BNDF QUANTITY='GAUGE HEAT FLUX'/

&SLCF QUANTITY= 'HRRPUV', PBX=0.165/

&SLCF QUANTITY= 'HRRPUV', PBY=0.955/

&DEVC XB=0.16,0.16,0.96,0.96,0.06,2.4, QUANTITY='HRRPUL', POINTS=70, Z_ID='Height', ID='HRRPUL' /
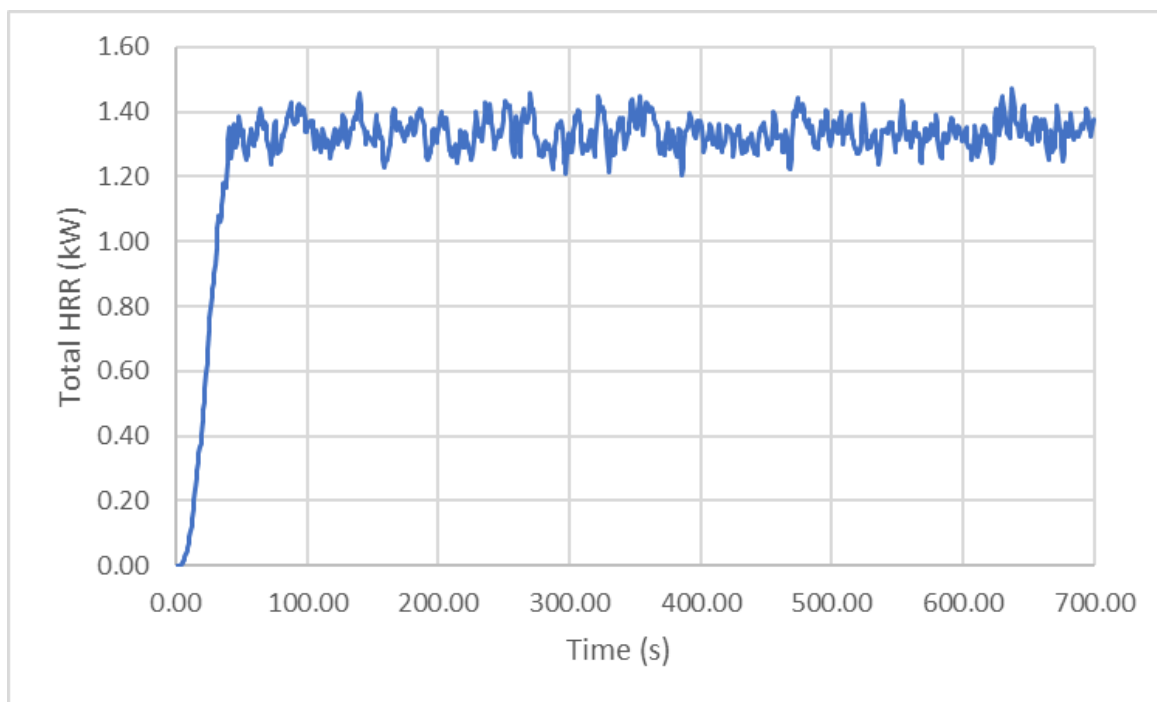

&TAIL /

9.2 DNS Total Heat Release Rate

Figure 21 Total HRR for DNS simulations. This result is consistent with each cell size
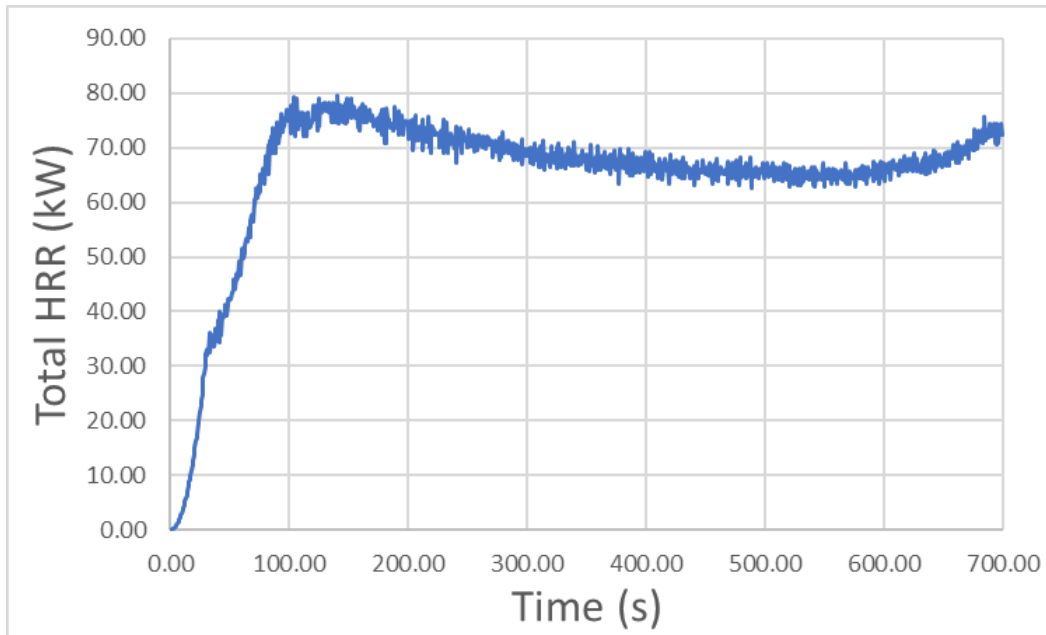
9.3   WALE Model Simulation Results

Figure 22 Total HRR of Plywood Simulation use WALE turbulence model. The cell size is 2cm with the heat of combustion of the pyrolysate being considered.
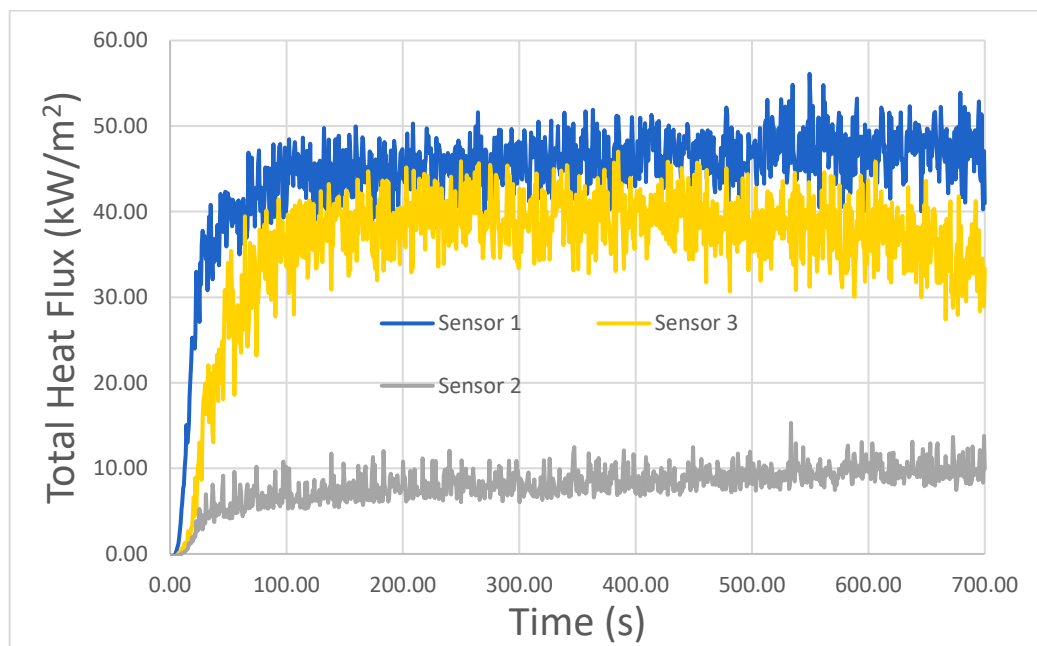

Figure 23 Predicted Total Heat Flux using WALE turbulence model